Physically-Based Simulation and Visualization of Optical Phenomena Elicited by Negative Refraction

by

Scott Steinfield

A thesis
presented to the University of Waterloo
in fulfillment of the
thesis requirement for the degree of
Master of Mathematics
in
Computer Science

Waterloo, Ontario, Canada, 2026

Author's Declaration

I hereby declare that I am the sole author of this thesis. This is a true copy of the thesis, including any required final revisions, as accepted by my examiners.

I understand that my thesis may be made electronically available to the public.

Abstract

Metamaterials characterized by a negative refractive index are being the object of intense research across a broad range of fields, from mathematics and physics to photonics and engineering. Nonetheless, the development of materials exhibiting this property in the visible spectral domain remains challenging. This situation, along with their potential transformative role in new technological advances, has motivated the scientific community to instrumentally employ computer graphics software to visually explore their interactions with light. In this work, we contribute to the initiatives in this area by describing a white-box methodology aimed at the physically-based simulation and visualization of optical phenomena elicited by these materials. We demonstrate its suitability to applications, both within and outside computer graphics, through the rendering of images depicting these phenomena under different optical scenarios, including those not examined in the literature to date.

Acknowledgements

I would like to thank the members of the Natural Phenomena Simulation Group: Petri Varsa, Francis Sun and Frank Fan for their support and the many great moments we shared along the way as well as Gabriel Baranoski for their assistance with the photography of Snell's Window. A special thanks to my supervisor, Gladimir Baranoski, for the many hours of guidance and encouragement that helped me to grow throughout this project. I would also like to thank the readers for their time and thoughtful review of this work.

Dedication

Dedicated to my family, particularly my amazing parents and my wonderful wife.

Table of Contents

List of Figures

List of Symbols

i When used as a subscript, the symbol i indicates incident. 8

$\vec{i}$ A vector that represents the direction of an incoming light ray. 8

$\vec{m}$ A vector that represents a unit tangent to an interface. 9

$\vec{n}$ A vector that represents a normal to a surface. 8

R Fresnel coefficient associated with quantity of reflected light at an interface. 17

R_{n_p} Fresnel coefficient associated with quantity of reflected light at an interface utilized by Persistence of Vision Ray Tracer. 65

$r_{\|}$ Fresnel amplitude coefficient associated with the parallel reflection of polarized light at an interface. 17

$r_{\perp}$ Fresnel amplitude coefficient associated with the perpendicular reflection of polarized light at an interface. 17

$\vec{r}$ A vector that represents the direction of a reflected light ray. 8

T Fresnel coefficient associated with quantity of transmitted light at an interface. 17

t When used as a subscript, the symbol t indicates transmitted. 8

$\vec{t}$ A vector that represents the direction of a transmitted light ray. 8

$\vec{t_n}$ A vector that represents the direction of a light ray transmitted into a NIM. 9

Z Wave impedance of a medium. 25

Z_i Wave impedance of medium where the illumination is incident. 30

Z_j Wave impedance of a generic medium that may represent where illumination is incident (i) or transmitted (t). 29

Z_t Wave impedance of medium where the illumination is transmitted. 30

Z_0 Wave impedance of vacuum. 29

ϵ Electric permittivity of a medium. 10

ϵ_r Relative electric permittivity. 10

ϵ_0 Electric permittivity of a vacuum. 10

η Refractive index of a medium. 11

η_i Refractive index for the medium where the illumination is incident. 9

η_t Refractive index for the medium where the illumination is transmitted. 9

η_{air} Refractive index of air. 14

η_{glass} Refractive index of glass. 13

η_{water} Refractive index of water. 13

θ_c Critical angle of incidence for total internal reflection to occur at an interface. 11

θ_i Angle of incident light measured between the surface normal and incident light ray. 8

θ_r Angle of reflected light measured from the surface normal to the reflected light ray. 8

θ_t Angle of transmitted light measured between the surface normal and transmitted light ray. 9

λ The wavelength of electromagnetic radiation (light). 11

μ Magnetic permeability of a medium. 10

μ_r Relative magnetic permeability. 10

μ_0 Magnetic permeability of a vacuum. 10

χ Uniformly distributed random number between 0 and 1. 32

$\perp$ Indicates perpendicular (s-polarized) component of light. 17

$\parallel$ Indicates parallel (p-polarized) component of light. 17

Chapter 1

Introduction

The physically-based modeling of material appearance has a pivotal importance for advanced computer graphics applications in different areas, from realistic image synthesis to the simulation and visualization of natural phenomena, just to name a few [38]. It has as its focal point the interactions of light (electromagnetic radiation) with distinct material components. These interactions, in turn, involve light absorption and scattering processes, which are often simulated using techniques, such as ray tracing and its variations (e.g., path tracing) [14, 25], based on geometrical (ray) optics [16], but also incorporating physical (wave) optics [21] concepts like the wavelength of light.

Ray tracing techniques have evolved considerably in the last decades. Still, their main core algorithms remain associated with the simulation of light propagation and attenuation mechanisms. The optical processes of light reflection and refraction, which are responsible for a myriad of striking visual effects found in nature (Figure 1.1), are integral components

of these mechanisms. Not surprisingly, their physically-based simulation, centered on use of well-established optical concepts and formulations, has been consistently incorporated into a large variety of appearance models.

These models are designed for materials (or media) that, despite their distinct appearance, can be characterized by a similar set of fundamental physical properties. These include their complex refractive index [16, 21], a radiometric quantity with two wavelength-dependent components: a real and an imaginary. The former, the relative refractive index (or simply referred to as the refractive index), is related to the phase velocity of a light wave propagating in a medium, *i.e.*, the ratio of the apparent speed of light in the vacuum to the speed in the medium. Basically, it determines how much light bends when transmitted into a medium. The latter, the extinction coefficient, is related to the attenuation of the wave. It determines how much light is absorbed in a medium.

In recent years, scientists and engineers started to pay more attention to a new class of materials, known as metamaterials (from the Greek word "meta", meaning "beyond" or "after"), that are artificially constructed to exhibit unconventional physical properties [44]. One of these properties refers to a negative refractive index as originally proposed by Veselago [52]. It has been acknowledged that materials with this property, termed NIMs (Negative-Index Materials) [45], can lead to the development of highly sophisticated technologies such as hyperlenses (capable of levels of magnification beyond the diffraction limit of light) [32, 34] and cloaking devices (capable of bending the light around objects so that they become invisible) [5, 43].

Figure 1.1: Photos illustrating riveting optical phenomena. Top: Distinct side and top-view photos of light reflection and refraction occurring in a glass containing a straw immersed in water. Middle: refraction of light through a crystal sphere resulting in caustic patterns. Bottom: refraction and total internal reflection of light at the ocean-air interface resulting in a Snell's window, which is partially depicted in the underwater photo.

Although significant progress has been achieved in the design of NIMs, published works in this area mainly report practical results involving the propagation of light in the infrared spectral domain and beyond. To date, the engineering of NIMs capable of openly enabling the aforementioned applications within the visible spectral domain remains elusive.

This aspect has led researchers from different fields [7, 9, 10, 30, 31, 39] to use computer graphics software, notably POV-Ray (Persistence of Vision Ray Tracer) [4, 37], to visualize phenomena prompted by negative refraction. We note, however, that this graphics resource was primarily employed instrumentally. Accordingly, their works abstained from providing detailed descriptions of the equations used to quantify the reflection and refraction of light by NIMs. Also, their visual depictions of material appearance changes resulting from light interactions with NIMs generally involved limited explorations of those equations' parameter space, overlooking variations in the materials' specific responses to electric and magnetic fields.

In this thesis, we focus on a physically-based methodology for the simulation and visualization of optical phenomena elicited by NIMs. Its formulation, based on the current understanding about these materials, is presented using a white-box approach. In other words, we describe the key optical equations employed to simulate negative refraction as well as the main mathematical and logical steps leading to them. Thus, researchers can analyze and seamlessly incorporate them in their own material appearance models and renderers not only to replicate our results, but also to pursue new avenues of theoretical and applied research in related areas of investigation. After all, as stated by Feynman [12], "Science is only useful if it tells you about some experiment that has not been done; it is

no good if it only tells you what just went on."

In short, the main contributions of this work are threefold. The described methods enable the predictive rendering of images depicting a broad range of optical scenarios involving light interactions with NIMs, including instances not yet examined in the literature and resulting from fresh explorations of the employed equations' parameter space. They also offer a robust basis for the modeling of NIMs' appearance traits. Lastly, they provide a physically-based platform for the *in silico* (computational) verification of hypotheses and algorithms associated with the NIMs' optical properties and their visual manifestations. Hence, we believe that the described methods and the phenomenological observations discussed in this work can benefit a wide gamut of applications, within and outside computer graphics, with distinct agendas, from educational and scientific purposes to entertainment and artistic uses.

The remainder of this thesis is organized as follows. In Chapter 2, we concisely review the key physical elements of this work's scientific substrate. In Chapter 3, we briefly examine related research initiatives. In Chapter 4, we describe the methods proposed for the physically-based simulation and visualization of optical phenomena elicited by NIMs. In Chapter 5, we assess the predictability and applicability of the the proposed methods. In Chapter 6, we conclude the thesis and outline directions for future research. Finally, in Appendices A and B, we provide supplemental information on relevant optical aspects.

Chapter 2

Physical Background

In this chapter, we provide a concise overview of the physical properties that affect the behaviour of light at an interface. We begin by discussing fundamental optical phenomena such as reflection, refraction and total internal reflection. We then examine a common occurrence for total internal reflection at the air-water interface, which gives rise to the optical phenomenon of a Snell's Window [28].

Building upon the previous discussion, we outline the Fresnel equations which quantify the fraction of light that is reflected and refracted at an interface between two materials. Finally, we extend our overview of light propagation of a conventional interface to an interface between a conventional material and a negative-index material (NIM), describing the resulting effects.

2.1 Light Propagation Overview

For completeness, in this section, we outline relevant optics concepts and terminology used in this work. Readers interested in more details about them are referred to comprehensive optics texts such as those employed as references [2, 16, 21] for this overview.

Consider the situation where light travels from a medium to another (e.g., from water to air). When it reaches the interface between them, its speed, direction and amplitude can change [21]. In this work, we focus on the how the light's direction is altered, eliciting a number of visual optical phenomena (e.g., see Sections 2.2 and 2.3).

At an interface between smooth materials, light can be reflected or refracted [16]. An illustration of this process is provided in Figure 2.1. We note that, throughout this work, we use $\vec{i}$, $\vec{r}$ and $\vec{t}$ to represent the incident, reflected and transmitted (light) rays, respectively. Similarly, the subscripts i and t correspondingly refer to the incidence and transmission media.

From fundamental optics [21], the law of reflection states that the angle of incidence θ_i is equal to the angle of reflection θ_r (Figure 2.1), with both angles being measured with respect to the interface's normal denoted by $\vec{n}$. Using this relationship, a reflected ray $\vec{r}$ can be computed as:

$$\vec{r} = \vec{i} + \vec{n}\cos\theta_i = \vec{i} - 2\vec{n}(\vec{i}\cdot\vec{n}). \tag{2.1}$$

Also from fundamental optics [21], the law of refraction, also known as Snell's law, states that:

$$\eta_i \sin\theta_i = \eta_t \sin\theta_t, \tag{2.2}$$

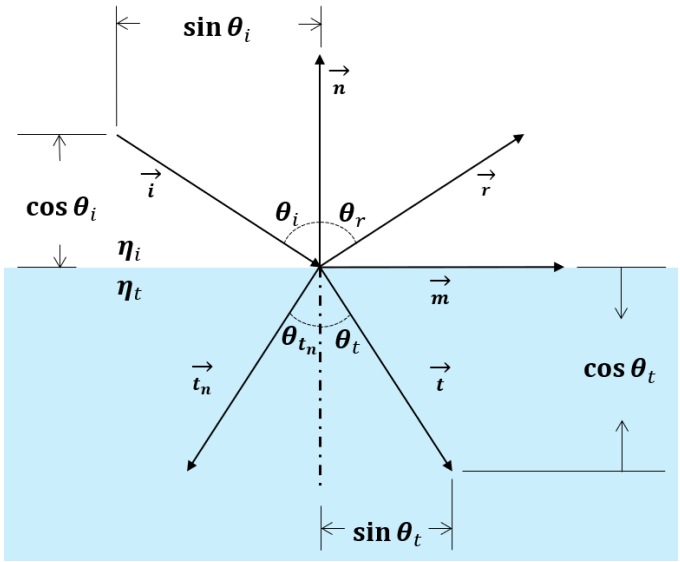

Figure 2.1: Geometry for light incident at the interface between two distinct materials (media). When the transmission medium has a negative refractive index ($\eta_t < 0$), the transmitted ray $\vec{t_n}$ appears on the same side of the normal $\vec{n}$ as the incident ray $\vec{i}$.

where η_i and η_t represent the refractive index of each medium. Similarly, using Snell's law, θ_t and $\vec{t}$ can be computed as:

$$\theta_t = \sin^{-1}(\frac{\eta_i}{\eta_t}\sin\theta_i) \tag{2.3}$$

and

$$\vec{t} = -\vec{n}\cos\theta_t + \vec{m}\sin\theta_t, \tag{2.4}$$

where $\vec{m}$ represents the vector tangent to the interface and perpendicular to $\vec{n}$.

Note that, as indicated by the Snell's law, the direction of light refraction associated

with the angle θ_t depends on the angle of incidence θ_i as well as on the refractive indices η_i and η_t. For example, if $\eta_i < \eta_t$, the light bends towards the normal. Otherwise, the light bends away from the normal direction.

Recall that light can be described as an electromagnetic wave and the refractive index quantifies a material's response to electromagnetic fields [21]. The refractive index, in turn, is related to the material's permeability μ and permittivity ϵ, which correspond to its responses to the magnetic and the electric fields, respectively [3].

In this work, we consider conventional materials classified as dielectrics (e.g., glass, air and water) as well as NIMs. The former are non-conducting and non-magnetic materials in the visible range. We also assume that both types of materials are isotropic, *i.e.*, their refractive index is the same at each point for light traveling in all directions (their permeability and permittivity are uniform in all directions) [16].

The refractive index of dielectrics under these assumptions can be represented considering their relative permeability μ_r and relative permittivity ϵ_r [21]:

$$\eta^2 = \mu_r \epsilon_r, \tag{2.5}$$

with μ_r and ϵ_r being expressed as:

$$\mu_r = \frac{\mu}{\mu_0} \tag{2.6}$$

and

$$\epsilon_r = \frac{\epsilon}{\epsilon_0}, \tag{2.7}$$

where μ_0 and ϵ_0 correspond to the permeability and permittivity of vacuum, respectively.

Note that Equation (2.5) has both a positive and a negative solution. As permeability, permittivity and the refractive index are known to be positive in dielectrics, we take the positive branch solution to get an expression for the latter:

$$\eta = \sqrt{\epsilon_r \mu_r}. \tag{2.8}$$

We remark that the permeability, permittivity and, thus, the refractive index of a medium are wavelength (λ) dependent quantities. For conciseness, this spectral dependence is omitted in the equations presented in this thesis. Furthermore, we assume that the examined light paths are reversible [21].

2.2 Total Internal Reflection

The Snell's law is associated with a myriad of optical phenomena elicited by the reflection and refraction of light at the interface between conventional media with distinct refractive indices. Through the inspection of Equations (2.2) and (2.3), it can be seen that as the angle of incidence θ_i increases, the angle θ_t also increases. Moreover, as θ_i increases, the transmitted ray $\vec{t}$ approaches a direction tangential to the interface represented by a vector $\vec{m}$ (Figure 2.1). In the case where $\eta_i > \eta_t$, there exists an angle of incidence for which $\vec{t}$ is parallel to $\vec{m}$, i.e., $\theta_t = 90°$, termed the critical angle (θ_c). Using Equation (2.2) and considering $\theta_t = 90°$, which results in $\sin\theta_t = 1$, the critical angle can be obtained as:

$$\theta_c = \sin^{-1}\left(\frac{\eta_t}{\eta_i}\right), \tag{2.9}$$

where $\eta_i > \eta_t$.

For any angle of incidence greater than the critical angle there is no refraction of light into the second (transmission) medium. All incoming energy is reflected back into the incidence medium. This phenomenon is known as the total internal reflection (TIR) [21]. The associated energy transfer is also quantified by the Fresnel coefficients obtained using Equations (2.11) to (2.14). Under the same condition ($\eta_i > \eta_t$), as θ_i increases, R also increases while T decreases [21].

A rendered illustration of TIR can be seen in Figure 2.2, which presents images based on a TIR demonstration case employed by Suffern [47]. The scene depicts a glass interface surrounded by water. For simplicity, we can consider the refractive index of water and glass represented by $\eta_{water} = 1.33$ and $\eta_{glass} = 1.5$, respectively [21]. In this situation, increasing the viewing angle across the four images (from the top-left, clockwise) effectively increases the angle of incidence as the light source remains fixed. We can observe that, for viewing angles approaching a nadir position, TIR becomes more evident at the bottom of the cube where the reflection of the sphere and sky are visible. Conversely, as the camera is moved toward the zenith position, we can observe refraction taking place at the bottom of the cube, i.e., TIR does not occur.

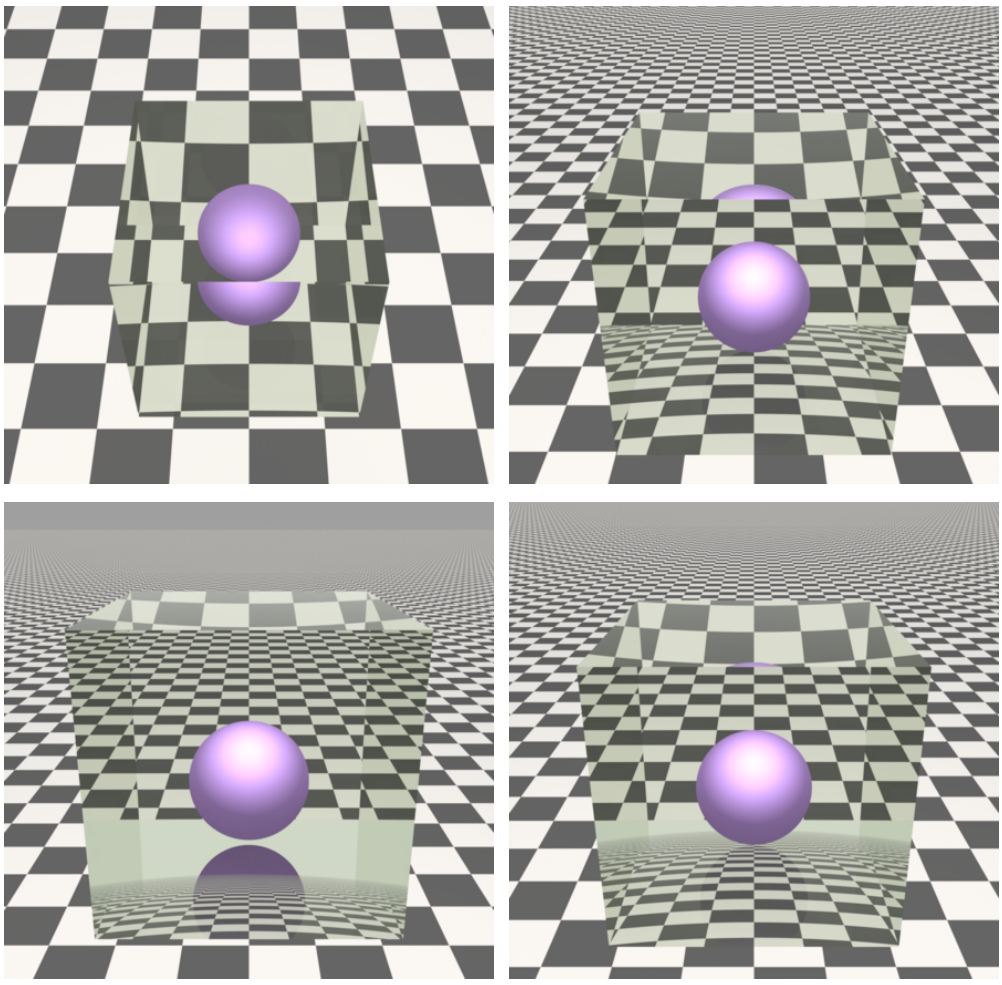

Figure 2.2: A series of images depicting a sphere inside of a glass cube. The glass has refractive index $\eta_{glass} = 1.5$, and it is surrounded by water with refractive index $\eta_{water} = 1.33$. The viewing angle increases as we move from the top-left to the bottom-left image. As a result, the reflection of the sky and sphere become visible near the bottom of the cube due to total internal reflection. The images were generated using the renderer and the stochastic techniques outlined in Section 4.3.

2.3 Snell's Window

A common setting for the occurrence of TIR in nature is at the interface between water and air. Also, for simplicity, we can consider the refractive index of air represented by $\eta_{air} = 1$ [21]. Since $\eta_{water} > \eta_{air}$, there exists a critical angle beyond which light traveling from water to air undergoes TIR. For this interface, where $\eta_i = 1.33$ and $\eta_t = 1$, we can calculate the critical angle using Equation (2.9):

$$\theta_c = \sin^{-1}(\frac{1}{1.33}) \approx 48.75^\circ. \tag{2.10}$$

The critical angle is also connected to another striking optical phenomenon schematically described in Figure 2.3. For an underwater observer, all light outside of a cone with an apex angle of $2 \cdot \theta_c \approx 97.5^\circ$ is totally internally reflected. This results in a circular window directly above the observer, through which the sky is visible. The full view of the sky is compressed within this window through refraction. A depiction of this phenomenon, known as Snell's window [28], is provided in the photo presented in Figure 1.1 (bottom). In the region surrounding a Snell's window, termed the Snell's blanket [28], light from below the air-water interface is totally reflected, preventing the underwater observer from seeing above the water surface.

It is worth noting that the Snell's window normally does not appear as a perfect circle for an underwater observer in the ocean. In this situation, ocean waves likely lead to the formation of rugged edges around the window's border [28]. These edges, in turn, prompt variations in the normal of the air-water interface, which alter the angle of light incidence. In deep ocean, since little light comes from below, the Snell's blanket appears dark. These

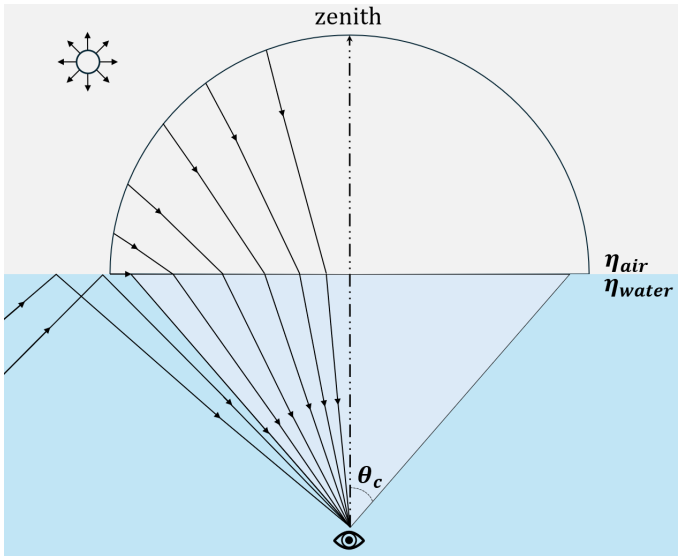

Figure 2.3: Diagram of a Snell's window at an interface between air ($\eta_{air} = 1.0$) and water ($\eta_{water} = 1.33$). As perceived by an underwater observer, the full view of the sky above the interface is compressed into a circular region. Total internal reflection takes place outside of a cone subtended by the critical angle (θ_c) [28].

aspects are illustrated in the images presented in Figure 2.4. It is worth noting that in a shallow swimming pool where the bottom is located only a few meters from the surface, the Snell's blanket can appear bright [28].

When the underwater observer is positioned at an offset angle rather than straight below, the cone of light forming the window projects onto the water surface at an angle, making the window appear elliptical rather than circular. This aspect is illustrated in the rendered image presented in Figure 2.4 (right). This shift to an elliptical shape is analogous

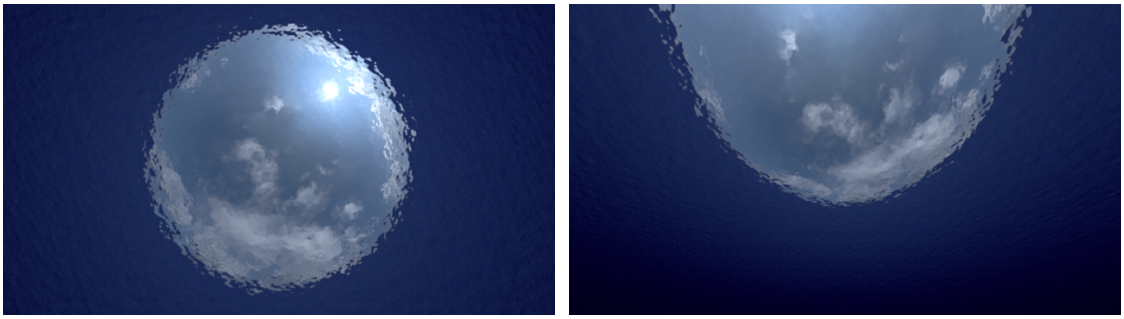

Figure 2.4: Images illustrating a Snell's window observed underwater from two viewing angles in the ocean. Left: observer's view direction is perpendicular to the air-water interface. Right: observer's view direction is oblique to the air-water interface. The images were generated using the renderer and the stochastic techniques outlined in Section 4.3.

to the one observed when shining a flashlight on a surface. When shone perpendicular to the surface, the light beam appears circular. When shone at an oblique angle, the light beam appears elliptical on the surface [14].

2.4 Fresnel Equations

When light encounters the interface between two convetional materials (media), a fraction of the wave's energy is refracted along $\vec{t}$ and the remainder is reflected along $\vec{r}$ [16] (Figure 2.1). The Fresnel equations [21] quantify the fractions of light that are reflected and refracted at the interface according to the angle of incidence, the refractive indices and light polarization (which indicates that the oscillations of its electrical field follow a specific

pattern [2]). The resulting quantities are commonly referred to as the Fresnel coefficients, denoted by R and T, respectively.

In this work, we consider unpolarized light, which corresponds to natural illumination with random changes in polarization [21]. To obtain R at the interface, we average the Fresnel amplitude reflection coefficients, denoted by r, in the perpendicular ($\perp$) and parallel ($\parallel$) directions with respect to the plane of incidence:

$$R = \frac{|r_\perp|^2 + |r_\parallel|^2}{2}, \tag{2.11}$$

where

$$r_\perp = \frac{\eta_i \cos\theta_i - \eta_t \cos\theta_t}{\eta_i \cos\theta_i + \eta_t \cos\theta_t}, \tag{2.12}$$

and

$$r_\parallel = \frac{\eta_t \cos\theta_i - \eta_i \cos\theta_t}{\eta_t \cos\theta_i + \eta_i \cos\theta_t}. \tag{2.13}$$

As the Fresnel equations describe the light behaviour at the interface, light absorption (extinction) is not considered. Thus, the fraction of incoming light that is not reflected at the interface is transmitted. Accordingly, considering the energy conservation principle [13], we can simply calculate T as:

$$T = 1 - R, \tag{2.14}$$

with R and T taking values varying from 0 to 1.

2.5 Negative-Index Materials

In 1968, Veselago theorized the existence of materials with μ_r, ϵ_r, $\eta < 0$ [52]. He believed that, if ever found, these materials would unveil unforeseen electromagnetic phenomena [36]. Although they could not have been found in nature to date, Pendry et al [35]. opened the possibility of engineering them three decades later. They proposed a variety of structures to reproduce the responses of Veselago's hypothesized materials and, for all practical purposes, initiated the quest for the development of NIMs [45]. In this section, we concisely introduce aspects associated with the representation of specific NIMs' optical responses relevant to this work.

Up until now, we have addressed conventional dielectric materials which are characterized by μ_r, ϵ_r, $\eta > 0$. As a result, the positive branch solution led to Equation (2.8). To obtain a negative refractive index, the negative branch solution of Equation (2.5) is considered so that:

$$\eta = -\sqrt{\epsilon_r \mu_r}. \tag{2.15}$$

Veselago's work laid the theoretical foundation for the exploration of NIMs [19]. In this thesis, we describe these materials as holding the parameters employed by Veselago [52]: μ_r, $\epsilon_r < 0$, with η calculated as indicated in Equation (2.15).

We can now examine light's behaviour at a new material interface between a conventional material and a NIM, henceforth referred to as a NIM interface. As stated by Pendry [34], Snell's law is still valid at an interface of this type. From Equation (2.3), we can see that in the case where $\eta_t < 0$, the resulting θ_t would actually be negative (θ_{t_n})and

the transmitted ray $\vec{t_n}$ would lie on the same side of the interface's normal as the incident ray $\vec{i}$. This phenomenon, known as negative refraction [21], is illustrated in Figure 2.1.

The Fresnel equations associated with a NIM interface require more detailed consideration, however. We address their derivation in Chapter 4.

Chapter 3

Related Work

The visual depiction of optical phenomena associated with light reflection and refraction by conventional materials has been widely covered in the computer graphics literature. For instance, the total internal reflection phenomenon has been depicted in computer generated images for several decades [9, 29, 47]. Thus, a review of this extensive body of work is beyond the scope of this investigation. Instead, in this chapter, we focus on relevant interdisciplinary initiatives specifically aimed at the visualization of optical phenomena elicited by materials exhibiting negative refraction.

Dolling et al. [10] were the first to use a computer graphics software, more specifically POV-Ray, [4, 37] for that purpose. They generated several images of a scene depicting a straw in a glass. They employed the images to compare appearance variations when considering the glass empty, filled with water and filled with a liquid NIM. However, they did not elaborate on the formulation employed to generate the images.

Courtial [7] was able to simulate negative refraction using lenslet arrays containing many small lenses. These arrays were placed in an arrangement that accounted for how each one focused incoming light. It allowed for the representation of interfaces with different refractive indices, including a NIM interface. Also using POV-Ray, Courtial employed this framework to generate images of a scene depicting a chess piece behind such an interface.

Danner et al. [8] generated images comparing the appearance of a swimming pool in the cases of being empty, holding water and holding a liquid NIM. They also used POV-Ray to generate their images without elaborating on the employed methodology.

Later on, Qui et al [39] presented images of a metamaterial magnifier. These images showed the magnification that occurs as a result of coating a mirror with a thin NIM shell. They stated that their images were produced using ray tracing techniques, but did not provide further details.

Subsequently, Naranjo-Correa et al. [31] used POV-Ray to produce an image of a transparent NIM sphere. They also presented illustrative diagrams to show the corresponding light paths for such an object. Their main purpose was to explore the didactic use of POV-Ray simulations and they did not discuss the underlying methodology used to obtain the image.

More recently, Naranjo-Correa and Martinez-Borreguero [30] presented images of a prism with a negative refractive index. Using a spectral rendering extension for POV-Ray, they demonstrated how NIM prisms disperse light across different wavelengths. However, their work also focused on educational demonstrations rather than on the underlying simulation methodology.

In summary, although existing related works have generated plausible images depicting optical phenomena elicited by negative refraction in specific optical scenarios, they have not comprehensively discussed the formulation employed to obtain them. In this thesis, we aim to contribute to the advance of investigations and applications involving this topic. We start, in the next chapter, by openly describing the methodology employed to achieve this goal.

Chapter 4

Methods

In this chapter, we present a set of equations that can be used to obtain the Fresnel coefficients required for the physically-based simulation and visualization of negative refraction phenomena using ray tracing techniques. We remark that their formulation builds on the knowledge foundation established by previous works on negative refraction and NIMs, which are cited where appropriate. While wave-optics parameters are considered, an in-depth theoretical examination of the Fresnel equations' physical roots and their boundary conditions are beyond the scope of this thesis. Readers interested in these aspects are referred to publications that specifically examine related wave optics concepts [19, 21, 46].

As suggested by Veselago [53], we utilize the wave impedance (denoted by Z), which determines the impedance an electromagnetic wave experiences as it travels through a material, to express Equations (6) to (8) in a more general form, i.e., without assuming that the target materials are non-magnetic. This allows for the consideration of electric

and magnetic effects as required for a NIM interface.

In order to incorporate the resulting equations into standard rendering pipelines, we subsequently re-express their wave impedance components in terms of refractive index. This is accomplished using the definitions of permeability and permittivity (Equations (3) and (4)), with considerations for the specific cases of conventional materials and NIMs.

We remark that, for interfaces between conventional materials and NIMs, we assume both to be isotropic, with the former being dielectrics having $\mu_r = 1$ [21], and the latter having μ, ϵ, $\eta < 0$ and $\mu_r = -1$ [52, 53], unless stated otherwise. We also reiterate that NIMs with these characteristics and capable of interacting with visible light have not been found in nature or manufactured yet as far as it can be inferred from published works in this area.

We conclude this chapter with a concise overview of implementation aspects associated with the rendering of images depicting optical phenomena brought about by negative refraction.

4.1 Fresnel Coefficients in Terms of Wave Impedance

As discussed previously, light incident at a NIM interface undergoes the phenomenon of negative refraction [21]. The Fresnel equations that we have referenced up until now are invalid at such an interface. More precisely, the Fresnel coefficients R and T computed using Equations (2.11) to (2.14) and considering a negative refractive index for the transmission medium may exceed 1, which violates the energy conservation principle (see Appendix A).

In order to effectively address this issue, it is necessary to revisit the employed equations. Gutiérrez and Stachura [19] reported that the equations used to calculate the Fresnel coefficients at a NIM interface differ slightly from the standard equations used for the conventional interfaces. Hence, special considerations need to be made for the case of negative refraction due to the unconventional direction of the transmitted (light) wave, as well as the fact that, in a NIM, the phase velocity is antiparallel to the direction of energy flow [53]. Also, the standard Fresnel equations assume that one is dealing with an interface of nonmagnetic materials $\mu_r = 1$ [21]. This is not the case at a NIM interface, where μ_r is negative for the transmitted medium [52].

As suggested by Veselago [53], since the nonmagnetic approximation no longer holds, we need to express the Fresnel equations in more general terms than those employed in Equations (2.11) to (2.13). These equations are derived under the assumption that $\mu_r = 1$, leading to $\eta = \sqrt{\epsilon_r}$ (Equation (2.8)) [21]. Also according to Veselago [53], one can maintain the Fresnel equations' theoretical basis by avoiding assumptions about the material's electromagnetic parameters and retaining their full generality. This is accomplished using wave impedance (Z) during the derivation, which combines a material's electric permittivity and magnetic permeability, resulting in a clean algebraic form. The assumption of $\mu_r = 1$ leading to $\eta = \sqrt{\epsilon_r}$ is replaced by:

$$\frac{1}{Z} = \sqrt{\frac{\epsilon_j}{\mu_j}} \tag{4.1}$$

where the subscript j refers to the incidence medium or the transmission medium. Note that the wave impedance remains positive for conventional materials and for NIMs [19, 53].

By retaining full generality of the electromagnetic parameters through wave impedance

during the derivation of the Fresnel equations [19, 53], we obtain the following Fresnel amplitude coefficients:

$$r_{\perp} = \frac{Z_t \cos\theta_i - Z_i \cos\theta_t}{Z_t \cos\theta_i + Z_i \cos\theta_t}, \tag{4.2}$$

and

$$r_{\parallel} = \frac{Z_i \cos\theta_i - Z_t \cos\theta_t}{Z_i \cos\theta_i + Z_t \cos\theta_t}. \tag{4.3}$$

These formulas are consistent with the ones provided by Gutiérrez and Stachura [19], differing only in convention choices. We now have the Fresnel equations expressed in a more general form, *i.e.*, with considerations for a NIM, avoiding assumptions about μ_r.

4.2 Fresnel Coefficients in Terms of Refractive Index

For integration into a standard rendering framework, we want to express Equations (4.2) and (4.3) in terms of the parameters η_i and η_t. Accordingly, the wave impedance of the incident and transmitted media can be expressed in terms of their refractive indices.

We note that wave impedance (Equation (4.1)) is expressed in terms of absolute permittivity (ϵ) and permeability (μ) while the refractive index (Equations (2.8) and (2.15)) is expressed in terms of the relative quantities (ϵ_r, μ_r). Note that these quantities are related by Equations (2.6) and (2.7), which are valid for both conventional materials and NIMs. Thus, we can re-express Equation (4.1) in terms of relative permittivity and permeability to get a form closer to Equations (2.8) and (2.15). First we note from Equations (2.6) and (2.7) that:

$$\mu = \mu_r \mu_0, \tag{4.4}$$

and

$$\epsilon = \epsilon_r \epsilon_0. \tag{4.5}$$

We then substitute Equations (4.4) and (4.5) into Equation (4.1) to obtain:

$$Z_j = \sqrt{\frac{\mu_{r_j}\mu_0}{\epsilon_{r_j}\epsilon_0}}. \tag{4.6}$$

Since $\frac{\mu_0}{\epsilon_0}$ and $\frac{\mu_{r_j}}{\epsilon_{r_j}}$ are positive (μ_{r_j} and ϵ_{r_j} have the same sign), we may separate the square root in the equation above in order to get:

$$Z_j = \sqrt{\frac{\mu_0}{\epsilon_0}}\sqrt{\frac{\mu_{r_j}}{\epsilon_{r_j}}}, \tag{4.7}$$

which further reduces to:

$$Z_j = Z_0\sqrt{\frac{\mu_{r_j}}{\epsilon_{r_j}}}, \tag{4.8}$$

where Z_0 is a constant calculated as $Z_0 = \sqrt{\frac{\mu_0}{\epsilon_0}}$.

Similarly, we can obtain Equation (4.8) expressed in a form closer to that indicated in Equations (2.8) and (2.15) by performing a few algebraic operations. We begin by multiplying by $\frac{\mu_{r_j}}{\mu_{r_j}}$ inside of the square root:

$$Z_j = Z_0\sqrt{\frac{\mu_{r_j}\mu_{r_j}}{\epsilon_{r_j}\mu_{r_j}}}. \tag{4.9}$$

Since the numerator and denominator in Equation (4.9) are both positive quantities we get:

$$Z_j = Z_0\frac{\sqrt{\mu_{r_j}\mu_{r_j}}}{\sqrt{\epsilon_{r_j}\mu_{r_j}}}. \tag{4.10}$$

Also, since $\sqrt{\mu_{r_j}\mu_{r_j}} = |\mu_r|$, we have:

$$Z_j = Z_0 \frac{|\mu_{r_j}|}{\sqrt{\epsilon_{r_j}\mu_{r_j}}}. \tag{4.11}$$

Note that Equation (4.11) is valid for both conventional materials and NIMs. Accordingly, it can be expressed in a separate form for each type of material. Hence, by re-expressing the denominator of Equation (4.11) according to Equation (2.8), we obtain:

$$Z_i = Z_0 \frac{|\mu_{r_i}|}{\eta_i}. \tag{4.12}$$

Similarly, by re-expressing the denominator of Equation (4.11) according to Equation (2.15), we get:

$$Z_t = -Z_0 \frac{|\mu_{r_t}|}{\eta_t}. \tag{4.13}$$

It is worth mentioning that both Equations (4.12) and (4.13) maintain a positive wave impedance, as emphasized by Gutiérrez and Stachura [19].

We can then substitute Equations (4.12) and (4.13) into Equations (4.2) and (4.3) to obtain an expression for the Fresnel equations at a NIM interface in terms of the refractive indices:

$$r_{\perp n} = \frac{-\frac{|\mu_{r_t}|}{\eta_t}\cos\theta_i - \frac{|\mu_{r_i}|}{\eta_i}\cos\theta_t}{-\frac{|\mu_{r_t}|}{\eta_t}\cos\theta_i + \frac{|\mu_{r_i}|}{\eta_i}\cos\theta_t}, \tag{4.14}$$

and

$$r_{\parallel n} = \frac{\frac{|\mu_{r_i}|}{\eta_i}\cos\theta_i + \frac{|\mu_{r_t}|}{\eta_t}\cos\theta_t}{\frac{|\mu_{r_i}|}{\eta_i}\cos\theta_i - \frac{|\mu_{r_t}|}{\eta_t}\cos\theta_t}. \tag{4.15}$$

By multiplying Equation (4.14) by $\frac{\eta_i\eta_t}{\eta_i\eta_t}$ and Equation (4.15) by $-\frac{\eta_i\eta_t}{\eta_i\eta_t}$, we get:

$$R_n = \frac{|r_{\perp n}|^2 + |r_{\parallel n}|^2}{2}, \tag{4.16}$$

where

$$r_{\perp n} = \frac{\eta_i \ |\mu_{r_t}| \cos\theta_i + \eta_t \ |\mu_{r_i}| \cos\theta_t}{\eta_i \ |\mu_{r_t}| \cos\theta_i - \eta_t \ |\mu_{r_i}| \cos\theta_t}, \tag{4.17}$$

and

$$r_{\parallel n} = \frac{\eta_t \ |\mu_{r_i}| \cos\theta_i + \eta_i \ |\mu_{r_t}| \cos\theta_t}{\eta_t \ |\mu_{r_i}| \cos\theta_i - \eta_i \ |\mu_{r_t}| \cos\theta_t}. \tag{4.18}$$

For practical convenience, unless otherwise stated, we make the following assumptions in this work. As suggested by Veselago [52, 53], we can consider $\mu_r = -1$ for NIMs. As for conventional materials, we consider $\mu_r = 1$ [21]. The Fresnel equations for a NIM interface can then be formulated with the components of Equation (4.16) expressed as:

$$r_{\perp n} = \frac{\eta_i \cos\theta_i + \eta_t \cos\theta_t}{\eta_i \cos\theta_i - \eta_t \cos\theta_t}, \tag{4.19}$$

and

$$r_{\parallel n} = \frac{\eta_t \cos\theta_i + \eta_i \cos\theta_t}{\eta_t \cos\theta_i - \eta_i \cos\theta_t}. \tag{4.20}$$

Again, considering the energy conservation principle [13], we can calculate T_n as:

$$T_n = 1 - R_n, \tag{4.21}$$

with R_n and T_n taking values varying from 0 to 1.

Hence, given unpolarized light incident at an interface between a conventional (right-handed) material and a NIM (left-handed) [41], Equations (4.16) to (4.21) can be used to properly estimate the corresponding reflection and transmission quantities (see Appendix A).

4.3 Implementation Aspects

To generate images depicting visual phenomena elicited by NIMs, one can employ a Monte Carlo path tracing algorithm [14, 25]. Accordingly, the reflection and transmission of light at a NIM interface is probabilistically determined using R_n given by Equation (4.16). More specifically, analogous to standard cases involving conventional materials, a random number χ uniformly distributed between 0 and 1 is generated. If $\chi < R_n$, then the incident light (ray) is reflected. Otherwise, it is transmitted (refracted).

In this work, we implemented the described methods as a custom plugin using the Mitsuba 3 renderer [23, 33]. We then employed it to generate the images presented in the next chapter. Furthermore, to facilitate the comparisons involving the optical phenomena depicted in those images, we considered a single representative value for the refractive index of the target materials across the visible spectral domain.

Chapter 5

Results and Discussion

In this chapter, we present the simulated results obtained from utilizing the methodology discussed in Section 4.3. Ideally, to demonstrate that simulations are predictive, one needs to evaluate their fidelity, *i.e.*, the degree to which they can reproduce the state or behaviour of a real object in a measurable or perceivable manner [18]. However, the engineering of real NIMs acting in the visible spectral domain has not been reported in the literature to date, which prevents direct quantitative comparisons with simulated NIMs.

Due to this practical constraint, we begin by focusing on qualitative aspects that have been visually or analytically identified in previous works by considering typical optical scenarios (baseline cases). More specifically, we generated images depicting these scenarios so that we could verify those qualitative aspects as well as the corresponding appearance differences between conventional materials and NIMs. We then complement our observations by considering additional related scenarios (complementary cases) which further

highlight key observations from the baseline cases. Finally, we showcase the applicability of the discussed methods by exploring the captivating optical scenario of a Snell's window under varying illumination conditions.

5.1 Baseline Cases

In Figures 5.1 and 5.2, we present images of a scene depicting a straw in a glass ($\eta = 1.5$) surrounded by air. These images illustrate the contrast in appearance between a straw inside of an empty glass, a glass containing water ($\eta = 1.33$) and a glass containing a liquid NIM ($\eta = -1.33$), from left to right, respectively. The images in 5.1 were obtained considering a side-view while the images in 5.2 considered a top-view.

We first examine the side-view images in Figure 5.1. We can note that the straw segment immersed in water appears slightly broken towards the left-hand side at the interface (Figure 5.1 (middle)), while it appears broken towards the right-hand side when immersed in the liquid NIM (Figure 5.1 (right)). Also, we remark that light rays entering the liquid NIM through the side of the glass are transmitted upwards, instead of downwards (Figure 2.1). This prompts several additional features, namely the bottom of the glass is no longer visible and the underside of the liquid NIM's surface is visible from the side of the glass as a "curved lip". All these features were also depicted in the images generated by Dolling *et al.* [10] for a similar scene with a straw immersed in water and in a liquid NIM.

Subsequently, examining the top-view images presented in Figure 5.2 (top-right and bottom-right), we can note a magnification of the straw segment immersed in the liquid

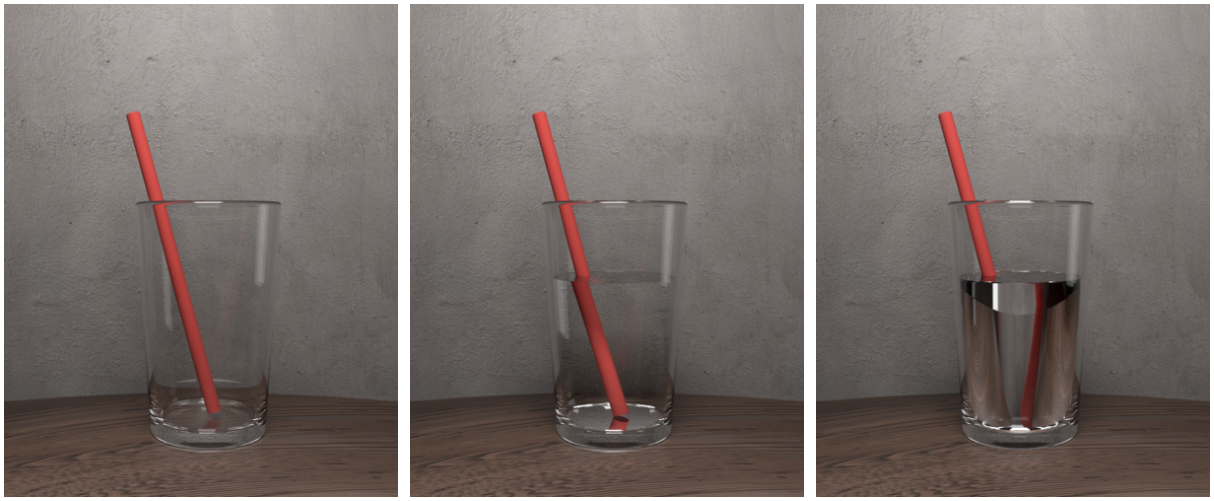

Figure 5.1: A sequence of side-view images depicting an empty glass with $\eta = 1.5$ (left), a glass containing water with $\eta = 1.33$ (middle) and a glass containing a liquid NIM with $\eta = -1.33$ (right).

NIM that varies with depth below the interface. In particular, the bottom end of the straw appears larger and slightly distorted towards the viewer. Moreover, the texture pattern of the table shown underneath the glass also appears magnified when compared to the top-view images showing the straw immersed in water (Figure 5.2 (top-middle and bottom-left)). Although Dolling *et al.* [10] did not provide top-view images of their glass-straw scene, they analytically indicated that such magnification and distortion effects can occur.

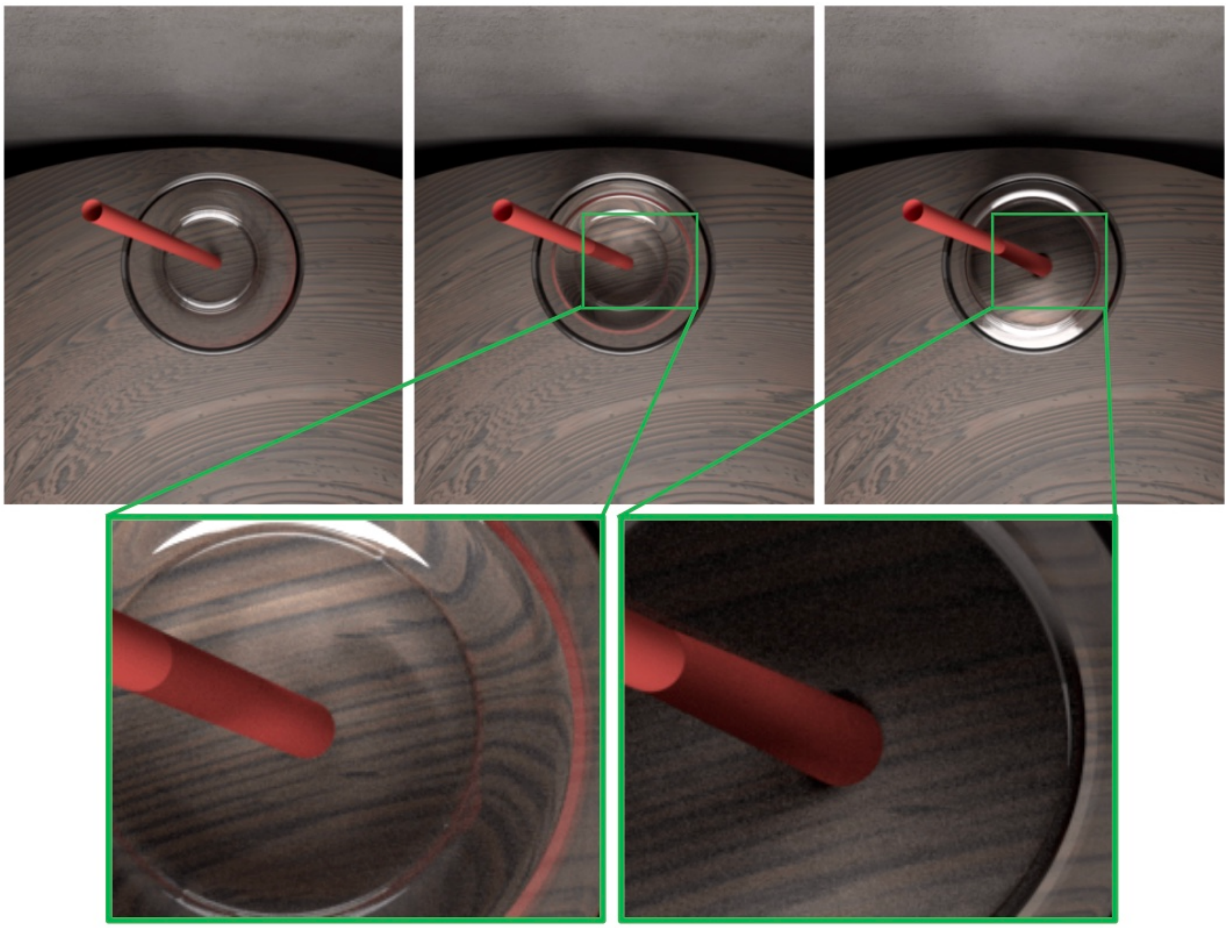

Figure 5.2: A sequence of top-view images depicting an empty glass with $\eta = 1.5$, a glass containing water with $\eta = 1.33$ and a glass containing a liquid NIM with $\eta = -1.33$ (top row) with corresponding zoomed-in images of the indicated regions for the cases of a glass containing water with $\eta = 1.33$ (bottom row, left) and a liquid NIM with $\eta = -1.33$ (bottom row, right).

In Figure 5.3, we present images of a scene depicting a swimming pool empty, holding water ($\eta = 1.33$) and holding a liquid NIM ($\eta = -1.33$) in the left, middle and right columns, respectively. The images in the left and middle columns serve as a references for the conventional appearance of the pool. The top row presents side-view images of the pool, allowing for comparisons with a similar scene employed in a liquid NIM simulation by Danner [8], while the bottom row presents top-view images.

Again, we start by examining the side-view images of the pool. While the interior edges and walls are not visible when the pool is holding water, they become visible when it is holding the liquid NIM. These observations aligned with those reported by Danner [8]. Moreover, examining the top-view images presented in Figure 5.3 (bottom row), we can perceive an apparent magnification of the pool floor below the liquid NIM, which is consistent with the analytical inferences of Dolling *et al.* [10] about this effect.

In Figure 5.4, we present images of a scene depicting a transparent sphere. These images were obtained considering the sphere made of different materials with distinct refractive indices. More precisely, the top-left image, used as reference, shows a glass sphere with a positive refractive index ($\eta = 1.5$). The other images, from top-right to bottom-left, show NIM spheres with distinct negative refractive indices ($\eta = -1.5$, $\eta = -1.33$ and $\eta = -1.025$, respectively).

For context, we first consider the image of the glass sphere (Figure 5.4 (top-left)). Incident light rays across the sphere's surface converge to form a caustic pattern. These converging rays also result in the background sky and ground appearing inverted (both vertically and horizontally) inside the sphere. These inversions can also be observed in the

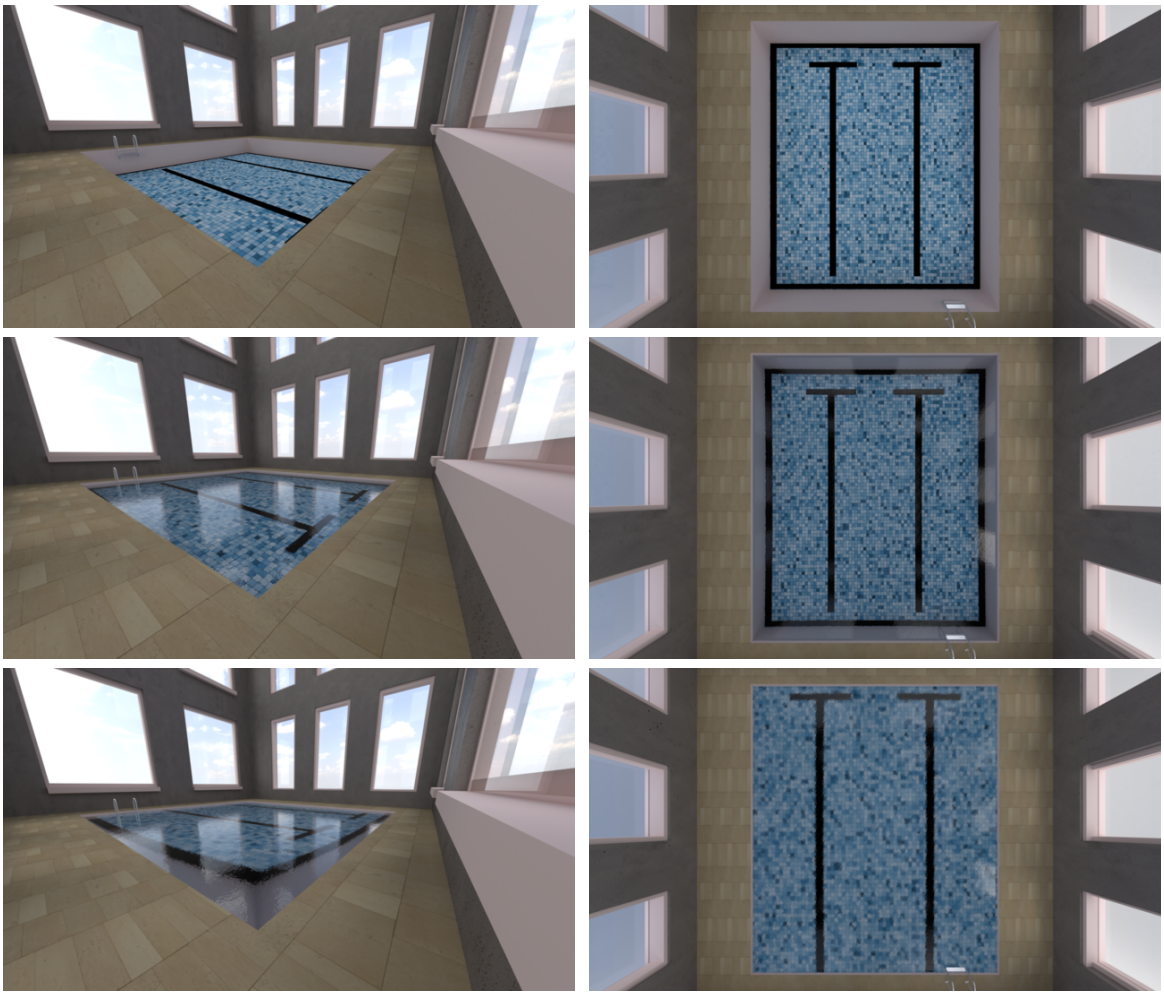

Figure 5.3: Side-view (left column) and top-view (right column) images of a swimming pool that is empty (top row), filled with water ($\eta = 1.33$; middle row) and filled with a liquid NIM ($\eta = -1.33$; bottom row).

photo of a real glass sphere presented in Figure 1.1 (top).

Proceeding to the images depicting the NIM spheres (Figures 5.4 (top-right), (bottom-right) and (bottom-left)), we can observe noticeable differences with respect to the glass (conventional material) sphere. For instance, the NIM spheres appear to be split into an inner (central) and an outer (peripheral) region. While we can note inversions in the inner region, these inversions are not perceived in the outer region. As the absolute magnitude of the refractive indices for the NIM spheres decreases (from top-right to bottom-left), it can be seen that the inner region shrinks and the outer region grows correspondingly. In addition, the NIM spheres project a markedly reduced caustic pattern. These aspects were also apparent in the NIM sphere image generated by Naranjo-Correa *et al.* [31]. Besides these differences, we can also point out that the caustic pattern becomes less noticeable as we considered negative refractive indices with a lower magnitude (approaching to -1). Such a refractive index variation also resulted in an expansion of their perceived outer region.

The above mentioned differences between the conventional and the NIM spheres are associated with the divergence of the lights rays traversing the NIM spheres. By employing ray diagrams (see Appendix B), it can be shown that light rays that hit these spheres on a central region emerge from the opposite hemisphere, while the others emerge from the same (incidence) hemisphere. Thus, the central region of the NIM spheres shows the scene background, while their peripheral regions show the foreground. These aspects were also depicted in the NIM sphere image generated by Naranjo-Correa *et al.* [31].

Figure 5.4: Images depicting transparent spheres with different refractive indices. From the top-left, clockwise, the refractive indices of the transparent spheres correspond to: $\eta = 1.5$, $\eta = -1.5$, $\eta = -1.33$ and $\eta = -1.025$.

5.2 Complementary Cases

In Figure 5.5, we present images depicting a scene composed of a glass, a green bunny placed behind the glass and two bunnies (a red and a blue) placed between the glass and the viewer. While the glass contains water ($\eta = 1.33$) in the left image, it contains a liquid NIM ($\eta = -1.33$) in the right image. As we can observe in the right image, the table surface in the foreground (in front of the glass) is visible near the edges of the liquid NIM. This can also be observed in the straw-glass image presented in Figure 5.1 (right). Moreover, the red and blue bunnies appear in the off-centre regions of the liquid NIM, while the green bunny remains visible through the centre of the glass, albeit flipped horizontally and distorted. These observations further highlight the qualitative aspects examined earlier.

In Figure 5.6, we present images depicting a variant of the optical scenario examined in Figure 5.4. More precisely, they show a modified scene composed of a transparent and two opaque spheres. While the transparent sphere was assigned a positive refractive index ($\eta = 1.5$) in the top-left image, it was assigned negative refractive indices in the other images.

As shown in the images presented in Figure 5.6 (top-right to bottom-left), the red sphere (placed behind the NIM spheres) appears only in the central region of the NIM spheres and in a reduced size. In addition, the blue sphere (placed in front of the NIM spheres) appears in the peripheral region of the NIM sphere. These features, which are also associated with the divergence of the rays propagated by the NIM spheres (see Appendix B), are significantly distinct from those observed for the glass sphere (Figure 5.6 (top-left)) and

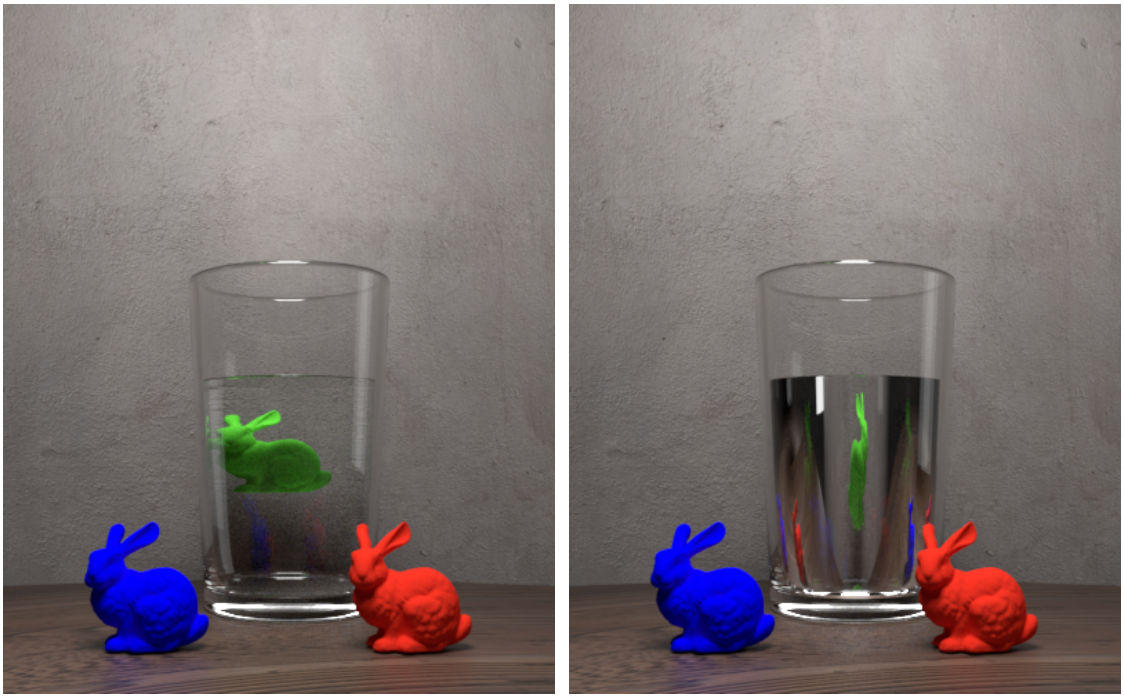

Figure 5.5: Images depicting a glass with $\eta = 1.5$ containing water with $\eta = 1.33$ (left) and a liquid NIM with $\eta = -1.33$ (right). The scene also includes a bunny (green) placed behind the glass and two bunnies (red and blue) placed in front of the glass.

consistent with those depicted in the NIM sphere image generated by Naranjo-Correa *et al.* [31].

We can further observe that the NIM spheres' outer regions shrink as we considered increasingly larger (magnitude wise) negative refractive indices ($\eta = -1.5$, $\eta = -2.418$ and $\eta = -4.1$, from top-right to bottom-left, respectively). Moreover, upon a closer inspection of their upper and lower regions, we can notice an increasing blend between the sky and

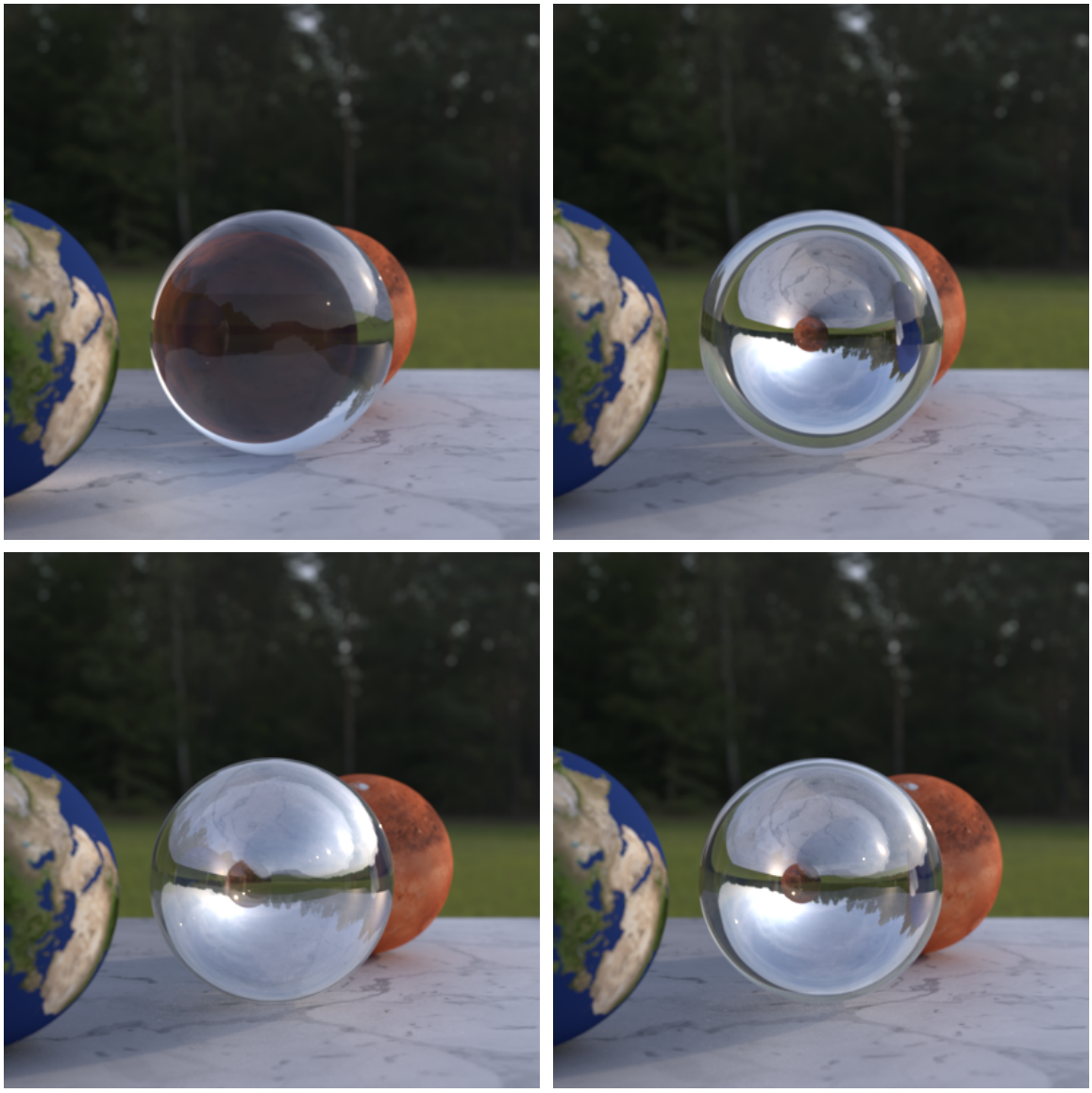

Figure 5.6: Images depicting transparent spheres surrounded by opaque spheres. From the top-left, clockwise, the refractive indices of the transparent spheres correspond to: $\eta = 1.5$, $\eta = -1.5$, $\eta = -2.418$ and $\eta = -4.1$.

ground surface with increasingly negative refractive indices being depicted within the NIM spheres.

5.3 Showcasing Applicability

In the previous section, we were able to qualitatively assess the predictability of the proposed methods. That provided us with a sound basis to showcase their broad applicability range in this section by examining optical scenarios overlooked in the related literature.

In Figure 5.7, we present images of a scene depicting a swimming pool, holding water (top) and a liquid NIM (bottom), during an overcast day. Different from the previously examined test cases (e.g., the scene depicted in Figure 5.3), this optical scenario provides the perspective of an observer (viewer) positioned inside of a medium (in this case, water with $\eta = 1.33$ or a liquid NIM with $\eta = -1.33$) with a refractive index whose magnitude is larger than that of the medium (in this case, air with $\eta = 1.0$) where the illumination source is located. The Snell's window phenomenon can then take place (see Section 2.3). More specifically, in this case, objects above the liquid surface are visible within a central region of the observer's field of view. This region, in turn, is surrounded by an outer region, the Snell's blanket, where the pool floor is reflected. Note that the circumference of the Snell's window is not perfectly circular since we accounted for the relative geometrical irregularity of the liquid surface due to external factors (e.g., wind).

In Figure 5.8, we present ray diagrams that delineate the light paths associated with the phenomena depicted in the images presented in Figure 5.7. In each diagram, we note

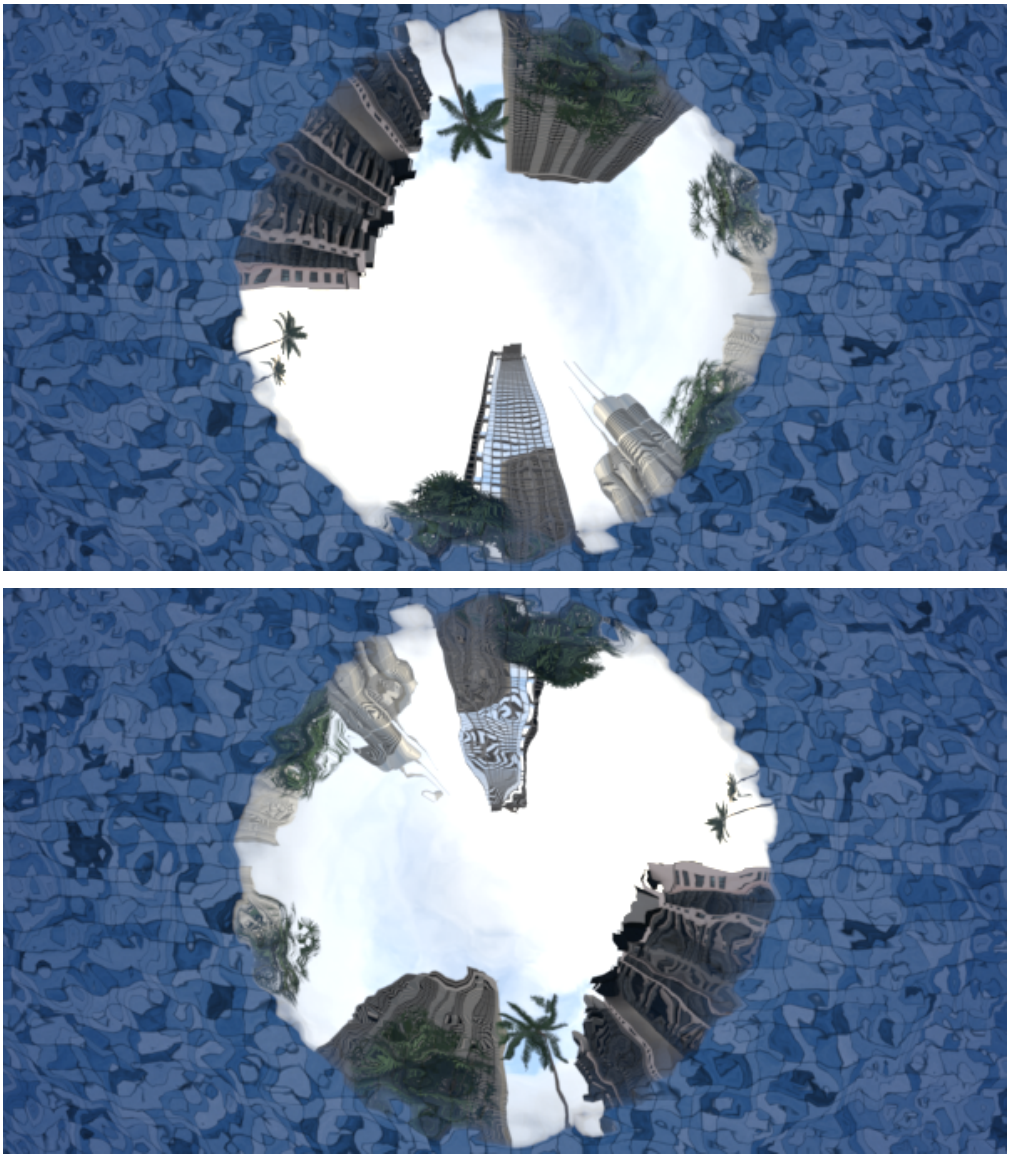

Figure 5.7: Images depicting the occurrence of a Snell's window in a swimming pool holding water with $\eta = 1.33$ (left) and a liquid NIM with $\eta = -1.33$ (right) during an overcast day.

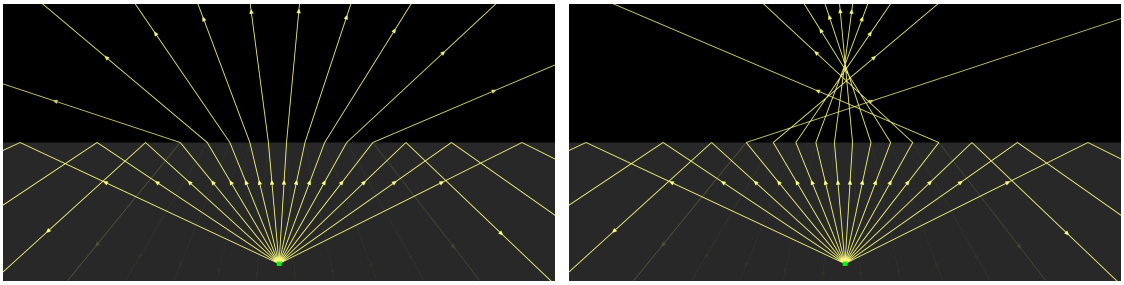

Figure 5.8: Ray diagrams computed for the scenes depicted in Figure 5.7. Left: swimming pool holding water ($\eta = 1.33$). Right: swimming pool holding a liquid NIM ($\eta = -1.33$). The diagrams were obtained using the Ray Optics Software [50].

that the central region of the air-liquid interfaces predominately transmits light, while regions outside of the critical angle undergo total internal reflection. We also note that, in the images and diagrams, the size of the Snell's blanket is consistent for both liquids. This is expected since the computation of a critical angle (see Section 2.2) for interfaces between materials (media) with the same magnitude refractive indices, such as the air-water ($\eta = 1.33$) and air-liquid NIM ($\eta = -1.33$) interfaces represented in Figure 5.7 and Figure 5.8, will result in equivalent values. We also remark that the Snell's law used in the critical angle computation remains valid for NIMs [34].

While the geometry of light reflection is the same for the air-water and air-liquid NIM interfaces, the geometry of light transmission is not as indicated by the ray diagrams presented in Figure 5.8. They show that there are noticeable differences in the paths of the rays traversing these interfaces. For instance, we can notice that the transmitted rays

diverge at the air-water interface as expected [21], while they converge at the air-liquid NIM as predicted by Veselago [52]. These differences contribute to the contrast between the two images, with the objects above the air-liquid NIM interface appearing distorted and mirrored across the Snell's window (Figure 5.7 (bottom)) when compared to those above the air-water interface (Figure 5.7 (top)).

In Figure 5.9, we present images depicting the same swimming pool scene during a sunny day, with the Snell's window occurring in an air-water interface (top image) and in an air-liquid NIM interface (bottom image). The increased brightness propagated through the interface leads to the projection of caustic patterns on the pool floor. These patterns are then reflected on the Snell's blanket. Due to the NIM's light converging and diverging behaviour [52], the patterns observed in the left and right images differ.

We remark that all previous images were generated considering the relative (magnetic) permeability of the conventional materials and NIMs given by $\mu_r = 1.0$ and $\mu_r = -1$, respectively. We note, however, that variations in the NIM's relative permeability can lead to changes in the magnitude of the Fresnel coefficients (see Appendix A). These changes, in turn, can alter the quantity of light reflected and transmitted at a NIM interface. To illustrate this aspect, in Figure 5.10, we present images depicting the swimming pool during an overcast day, but holding liquid NIMs characterized by relatively large magnitude (negative) values for the relative permeability, namely $\mu_r = -10$ (top image) and $\mu_r = -25$ (bottom image). With more light being reflected for larger magnitude μ_r values, less light is transmitted through the interfaces, darkening the scene and revealing the pattern of the pool floor within the Snell's window. This can be noticed when comparing the images

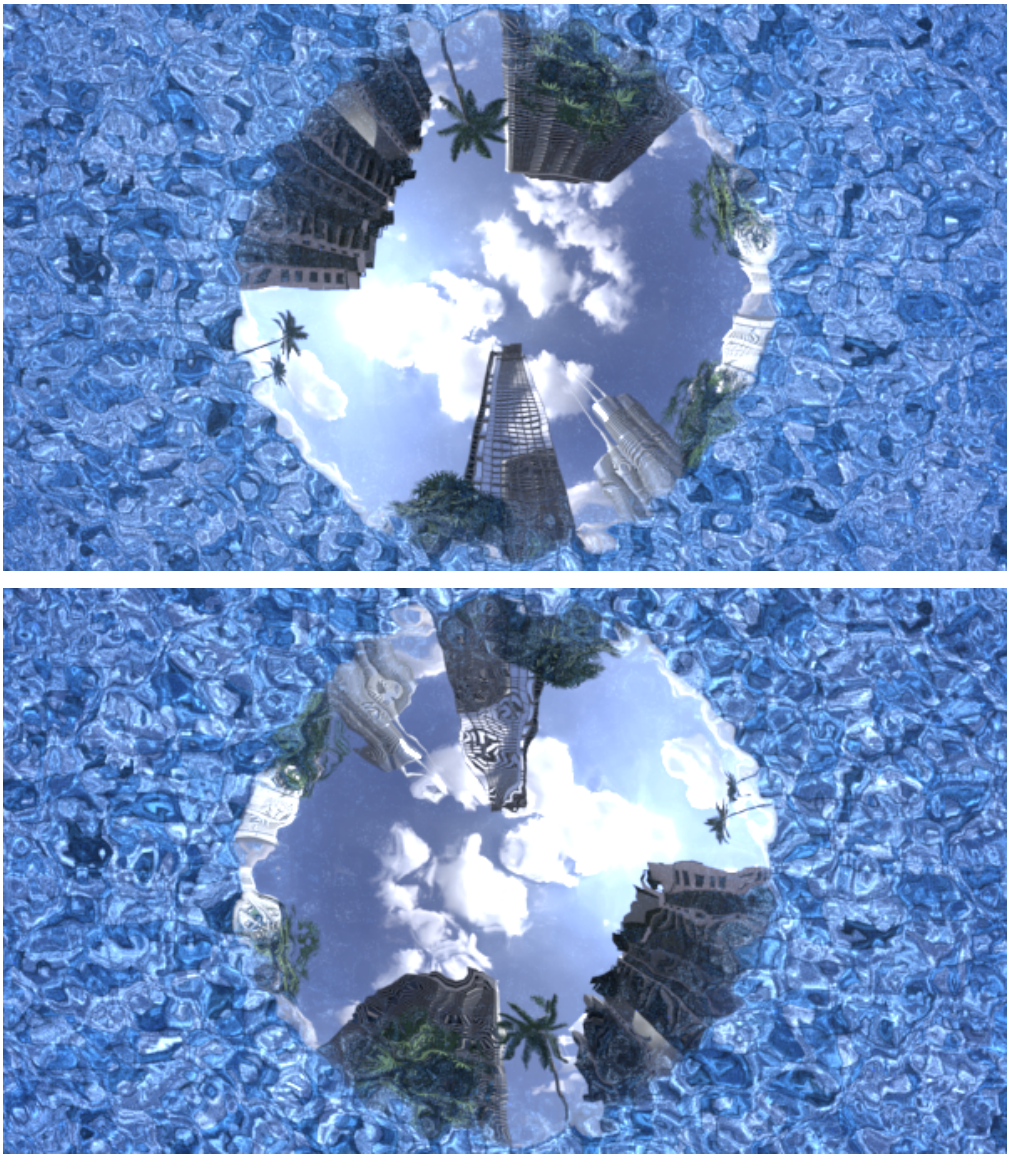

Figure 5.9: Images depicting the occurrence of a Snell's window in a swimming pool holding water with $\eta = 1.33$ (top) and a liquid NIM with $\eta = -1.33$ (bottom) during a sunny day.

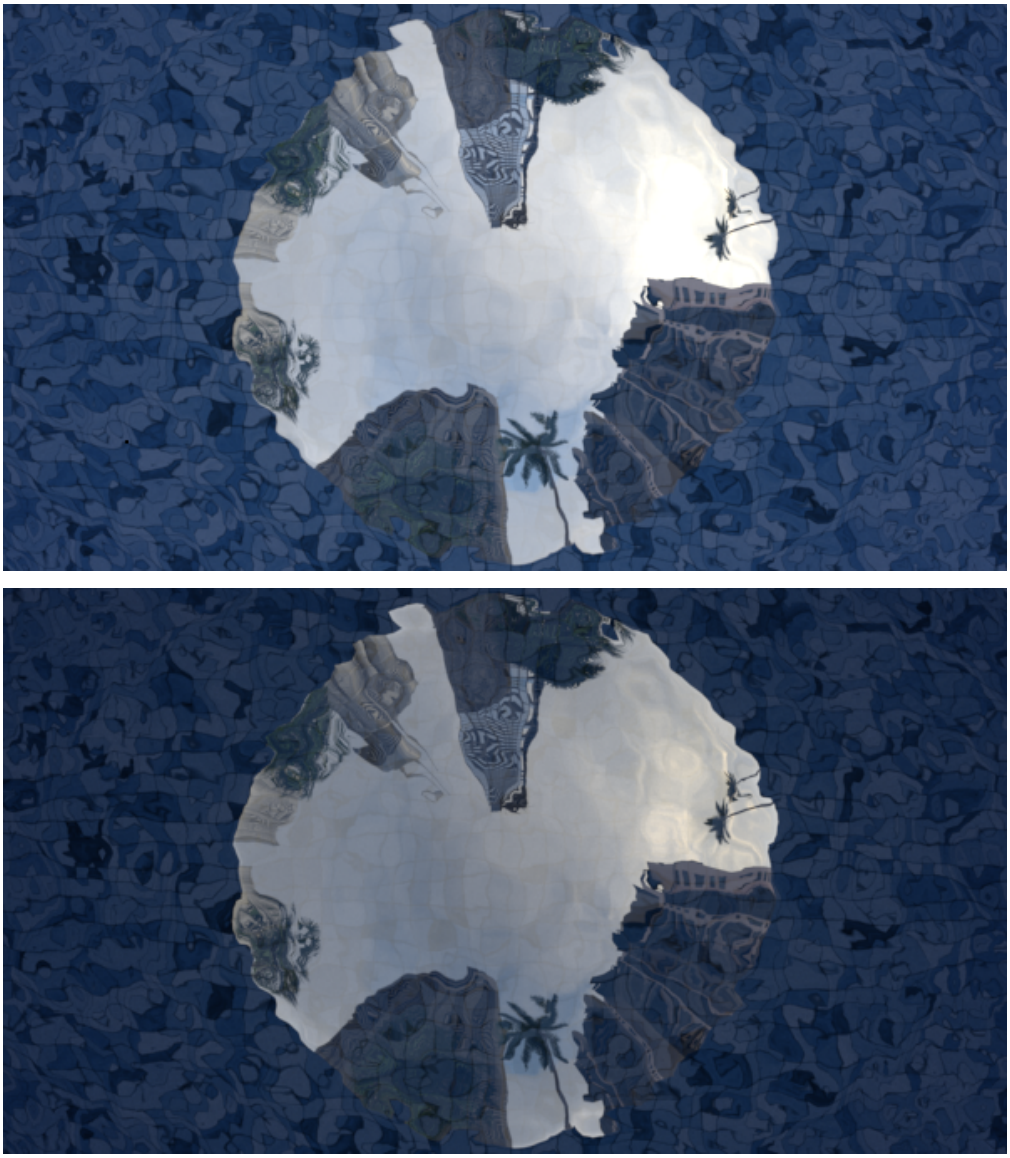

Figure 5.10: Images depicting a Snell's window in a swimming pool during an overcast day with the observer immersed in NIMs with the same refractive index ($\eta = -1.33$) and distinct relative magnetic permeabilities: $\mu_r = -10$ (top) and $\mu_r = -25$ (bottom).

presented in Figure 5.10 with the image presented in Figure 5.7 (bottom).

It is worth mentioning that the examined cases represent a small subset of all possible situations involving the simulation and visualization of material appearance changes elicited by negative refraction. For conciseness, we focused on foundational optical scenarios. Nonetheless, further variations in the characterization parameters and shape of NIMs, along with different viewing and illumination arrangements, are expected to unveil a myriad of unexplored visual phenomena.

Chapter 6

Conclusion

Negative refraction is a topic of great interest for theoretical and applied science initiatives across different fields. Despite advances in this line of research, real life observations of phenomena elicited by NIMs in the visible spectral domain have not been reported in the literature to date. Instead, researchers from those fields have been resorting to computer graphics software to visualize these phenomena.

In this thesis, we aimed to bring this topic to the attention of the computer graphics community, notably with respect to its material appearance ramifications, and to present alternative simulation and visualization strategies for related interdisciplinary investigations. To achieve that, we carefully described the methods employed in this work and their parameter space. In this way, our *in silico* experiments and observations can be effectively replicated and expanded for applications in science, education, entertainment and arts.

Besides assessing the predictability of the described methods through the qualitative

inspection of results obtained considering typical optical scenarios, we also examine their plausibility with respect to optical scenarios offering a fresh perspective about the intertwined visual phenomena elicited by NIMs. These scenarios are by no means exhaustive examples of these phenomena, however.

As NIMs and their applications become gradually more ubiquitous, several avenues for future research involving these materials can be outlined. These include, but are not limited to, the visualization of the environmental effects of NIMs with special properties (e.g., superconductivity), the exploration of negative refraction as an alternative light propagation mechanism for existing and new appearance models used in realistic image synthesis, and the investigation of the role played by other wave parameters (e.g., phase) in this context. We believe that the pairing of sound physical theories with robust rendering techniques can play a central part in this pursuit of a deeper understanding about these intriguing materials.

References

[1] Rosa Mach Batlle. *Controlling Static Magnetic Fields with Positive and Negative Permeability Metamaterials*. PhD thesis, Universitat Autònoma de Barcelona, Bellaterra, Spain, June 2019.

[2] J.M. Bennett. Polarization. In M. Bass, E.W.V Stryland, D.R. Williams, and W.L. Wolfe, editors, *Handbook of Optics (Volume I: Fundamentals, Techniques, & Design)*, pages 6.1–6.21, New York. USA, 1995. Optical Society of America, McGraw-Hill, Inc. Ch. 6.

[3] C.G. Bohren. Scattering by particles. In M. Bass, E.W.V Stryland, D.R. Williams, and W.L. Wolfe, editors, *Handbook of Optics (Volume I: Fundamentals, Techniques, & Design)*, pages 5.1–5.30, New York, USA, 1995. Optical Society of America, McGraw-Hill, Inc. Chapter 6.

[4] D.K. Buck, A.A. Collins, and A. Enzmann. *Persistence of Vision Ray Tracer - Documentation*. POV-Team, 1991. https://www.povray.org/.

[5] W. Cai, U.K. Chettiar, A.V. Kildishev, and V.M Shalaev. Optical cloaking with metamaterials. *Nature Photonics*, 1(4):224–227, 2007.

[6] Manas Chanda. Magnetic Properties. In *Science of Engineering Materials*, pages 127–155. Macmillan Education UK, 1980.

[7] J. Courtial. Ray-optical refraction with confocal lenslet arrays. *New Journal of Physics*, 10:083033:1–8, 2008.

[8] J.A. Danner. Visualizing invisibility: Metamaterials-based optical devices in natural environments. *Optics Express*, 18(4):3332–3337, 2010.

[9] S.T. Davis and C. Wyman. Interactive refractions with total internal reflection. In *Proceedings of the Graphics Interface Conference*, pages 185–190, Montréal, Canada, May 2007.

[10] G. Dolling, M. Wegener, S. Linden, and C. Hormann. Photorealistic images of objects in effective negative-index materials. *Optics Express*, 14(5):1842–1849, 2006.

[11] J. Dorsey, H. Rushmeier, and F. Sillion. *Digital Modeling of Material Appearance*. Morgan Kaufmann/Elsevier, Burlington, USA, 2007.

[12] R.P. Feynman. *The Character of Physical Law*. The Modern Library, New York, NY, 1964.

[13] R.P. Feynman. *QED The Strange Theory of Light and Matter*. Princeton University Press, Princeton, New Jersey, 1985.

[14] A.S. Glassner. *Principles of Digital Image Synthesis*. Morgan Kaufmann Publishers, Inc, San Francisco, USA, 1995.

[15] B.B. Gnecco and M. P. Guimarães. Laje de Santos: a dive site recreated in virtual reality. In *Proceedings of the Symposium on Virtual and Augmented Reality*, pages 75–82, Natal, Brazil, October 2022.

[16] D.S. Goodman. General principles of geometrical optics. In M. Bass, E.W.V Stryland, D.R. Williams, and W.L. Wolfe, editors, *Handbook of Optics (Volume I: Fundamentals, Techniques, & Design)*, pages 1.3–1.109, New York, 1995. Optical Society of America, McGraw-Hill, Inc. Ch. 1.

[17] D.P. Greenberg, J. Arvo, E. Lafortune, K.E. Torrance, J.A. Ferwerda, B. Walter, B. Trumbore, P. Shirley, S. Pattanaik, and S. Foo. A framework for realistic image synthesis. In *SIGGRAPH, Annual Conference Series*, pages 477–494, 1997.

[18] D.C. Gross. Report from the fidelity implementation study group. In *Simulation Interoperability Workshop, Simulation Interoperability and Standards Organization*, Orlando, FL, USA, 1999. Paper 99S-SIW-167.

[19] C.E. Gutiérrez and E. Stachura. Uniform refraction in negative refractive index materials. *Journal of the Optical Society of America A*, 32(11):2110–2122, 2015.

[20] G.M. Hale and M.R. Querry. Optical constants of water in the 200-nm to 200-um wavelength region. *Applied Optics*, 12(3):555–563, 1973.

[21] E. Hecht. *Optics*. Pearson Education Limited, Essex, England, 5th edition, 2017.

[22] R.W.G. Hunt and M.R. Pointer. *Measuring Colour*. John Wiley & Sons, Chichester, United Kingdom, 4 edition, 2011.

[23] W. Jakob, S. Speierer, N. Roussel, M. Nimier-David, D. Vicini, T. Zeltner, B. Nicolet, M. Crespo, V. Leroy, and Z. Zhang. *Mitsuba 3 renderer*, 2022. https://mitsuba-renderer.org.

[24] W. Jakob, S. Speierer, N. Roussel, M. Nimier-David, D. Vicini, T. Zeltner, B. Nicolet, M. Crespo, V. Leroy, and Z. Zhang. Mitsuba 3 renderer, 2022. Version 3.0.1.

[25] J. Kajiya. The rendering equation. *Computer Graphics (SIGGRAPH Proceedings)*, 20(4):143–150, August 1986.

[26] R.S. Kshetrinayum. A brief intro to metamaterials. *IEEE Potentials*, pages 44–46, February 2005.

[27] C. Lilley, F. Lin, W.T. Hewitt, and T.L.J. Howard. *Colour in Computer Graphics*. ITTI Computer Graphics and Visualization, Manchester Computing Centre, The University of Manchester, Manchester, England, December 1993.

[28] D.K. Lynch. Snell's window in wavy water. *Applied Optics*, 54(4):B8–B11, 2015.

[29] N. Monzon, D. Gutierrez, D. Akkaynak, and A. Muñoz. Real-time underwater spectral rendering. *Computer Graphics Forum*, 43(2):1–11, 2024.

[30] F.L. Naranjo-Correa and G.Martinez-Borreguero. Educational simulations of spectral color dispersion in negative prisms. *Col. Res. Appl.*, 49:163–176, 2024.

[31] F.L. Naranjo-Correa, G.Martinez-Borreguero, A.L. Pérez-Rodriguez, P.J. Pardo-Fernandez, and M. Isabel Suero-Lopez. Teaching rainbows with simulations: revisiting Minaert's lab experiment. *Applied Optics*, 15(19):G59–G74, 2017.

[32] E.E. Narimanov and V.M. Shalaev. Beyond diffraction. *Nature*, 447:266–267, May 2007.

[33] M. Nimier-David, D. Vicini, T. Zeltner, and W. Jakob. Mitsuba 2: A retargetable forward and inverse renderer. *ACM Trans. Graph.*, 38(6):203:1–17, 2019.

[34] J.B. Pendry. Negative Refraction Makes a Perfect Lens. *Physical Review Letters*, 85(18):3966–3969, 2000.

[35] J.B. Pendry, A.J. Holden, D.J. Robbins, and W.J. Stewart. Magnetism from conductors and enhanced nonlinear phenomena. *IEEE Transactions on Microwave theory and Techniques*, 47(11):2075–2084, 1999.

[36] J.B. Pendry and D.R. Smith. Reversing light: negative refraction. *Physics Today*, pages 1–8, December 2003.

[37] Persistence of Vision Pty. Ltd. Persistence of vision raytracer. http://www.povray.org, 2004. Version 3.6.

[38] P. Poulin and H. Rushmeier. Material appearance. *IEEE Computer Graphics & Applications*, 32:22–23, 2012.

[39] C. Qiu, A. Akbarzadeh, T. Han, and A.J. Danner. Photorealistic rendering of a graded negative-index metamaterial magnifier. *New Journal of Physics*, 14:033024:1–10, 2012.

[40] A. L. Rakhmanov, V. A. Yampol'skii, J. A. Fan, Federico Capasso, and Franco Nori. Layered superconductors as negative-refractive-index metamaterials. *Phys. Rev. B*, 81:075101, 2010.

[41] R.A. Shelby, D.R. Smith, and S. Schultz. Experimental verification of negative refraction. *Science*, 292(April):77–79, 2001.

[42] M.L. Shendeleva. Caustics in a field negatively refracted at a plane interface. *Journal of Microscopy*, 229(3):452–456, 2008.

[43] P. Sheng. Waves on the horizon. *Science*, 313:1399–1400, September 2006.

[44] D.R. Smith, J.B. Pendry, and M.C.K. Wiltshire. Metamaterials and negative refractive index. *Science*, 305(August):788–792, 2006.

[45] C.M. Soukoulis, S. Linden, and M. Wegener. Negative refractive index at optical wavelengths. *Science*, 315(January):47–49, 2007.

[46] S. Steinberg. Analytic spectral integration of birefringence-induced iridescence. *Computer Graphics Forum*, 38(4):97–110, 2019.

[47] Kevin G. Suffern. Effective instructional animation in 3D computer graphics education. In *Proceedings of the Australasian Conference on Computing Education*, pages 228–234, Melbourne, Australia, 2000. ACM.

[48] Michael Tinkham. *Introduction to Superconductivity*. Dover Publications, Mineola, New York, 2 edition, June 2004.

[49] W.J. Tropf and M.E. Thomas. Properties of crystals and glasses. In M. Bass, C.M. DeCusatis, V. Lakshminarayanan, G. Li, C. MacDonald, V.N. Mahajan, and E.V. Stryland, editors, *Handbook of Optics (Volume IV: Optical Properties of Materials, Nonlinear Optics, Quantum Optics)*, pages 2:1–93, New York, NY, USA, 2010. McGraw-Hill, Inc. Chapter 2.

[50] Y. Tu et al. Ray Optics Simulation. https://phydemo.app/ray-optics/, 2016.

[51] R. van Aken. Single mode fiber to planar waveguide coupling with ball lenses. Master's thesis, Delft University of Technology, 1992.

[52] V.G. Veselago. The Electrodynamics of Substances with Simultaneously Negative Values of ϵ and μ. *Soviet Physics Uspekhi*, 10(4):509–514, 1968.

[53] V.G. Veselago. Electrodynamics of materials with negative index of refraction. *Physics-Uspekhi*, 46(7):764–768, July 2003.

APPENDICES

Appendix A

Fresnel Coefficients and Energy Conservation

The correct simulation of optical phenomena elicited by negative refraction requires the Fresnel equations to follow the energy conservation principle [13]. Let's consider a NIM interface whose incidence and transmission media have refractive indices equal to 1 and -1.5, respectively. As shown in the graph presented in Figure A.1, the use of the standard Fresnel formulation (Equations (2.11) to (2.13)) can result in coefficients greater than 1, violating that principle.

Thus, it becomes necessary to adjust the Fresnel equations such that they take into account the distinct features of a NIM interface (see Chapter 4). As indicated in the graph presented in Figure A.2, the amplitude reflection coefficients and the Fresnel coefficient (R_n) computed using the described formulation (Equations (4.16), (4.19) and (4.20)) obey

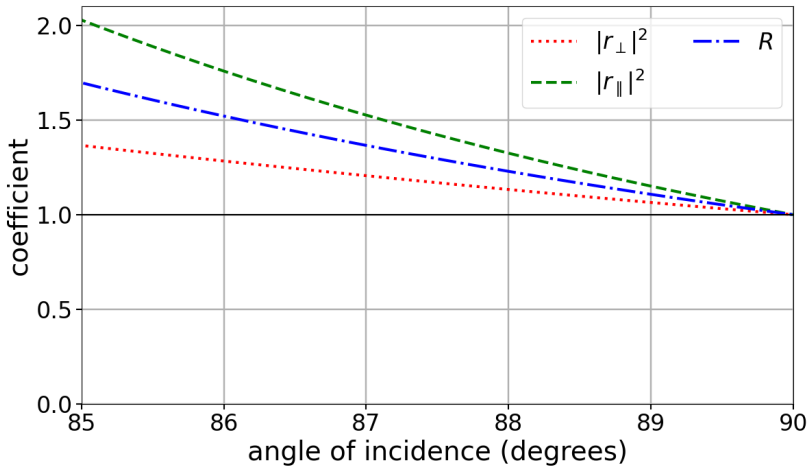

Figure A.1: Amplitude reflection coefficients ($|r_\perp|^2$ and $|r_\parallel|^2$) and the Fresnel coefficient R calculated for the specified NIM interface using Equations (2.11), (2.12) and (2.13).

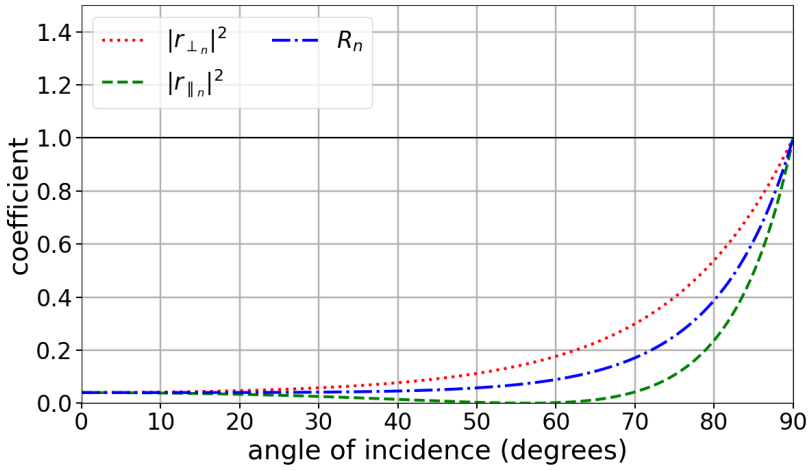

Figure A.2: Amplitude reflection coefficients ($|r_{\perp n}|^2$ and $|r_{\parallel n}|^2$) and Fresnel coefficient R_n calculated for the specified NIM interface using Equations (4.16), (4.19) and (4.20).

the energy conservation principle, i.e., they remain less than 1.

Recall that previous related works [7, 9, 10, 30, 31, 39] instrumentally employed POV-Ray [4, 37] in their negative refraction simulations. Upon inspecting the POV-Ray source code, it can be verified that it implements its own version of the Fresnel formulation. More specifically, the POV-Ray Fresnel coefficient, R_{n_p}, is calculated as follows:

$$R_{n_P} = \frac{1}{2}\left(\frac{g-c}{g+c}\right)^2\left[1+\left(\frac{c(g+c)-1}{c(g-c)+1}\right)^2\right], \tag{A.1}$$

where

$$c = \cos(\theta_i), \tag{A.2}$$

and

$$g = \sqrt{\left(\frac{\eta_i}{\eta_t}\right)^2 + \cos^2(\theta_i) - 1}. \tag{A.3}$$

The graph presented in Figure A.3 compares the values provided by R and R_{n_P} for different angles of incidence. It can be observed that the modified formulations produce identical results. However, the POV-Ray implementation of the Fresnel equations only allows the variation of the refractive index and the angle of incidence, *i.e.*, other key parameters, such as relative the (magnetic) permeability, are kept fixed.

The relative permeability (μ_r) measures the ability of a material to be magnetized by an applied magnetic field compared to a vacuum [6]. Metamaterials can produce a negative permeability according to their engineering [35], which exhibits unique properties not achievable with conventional positive-permeability materials. This process can lead to new tools for shaping, controlling and creating static magnetic fields [1].

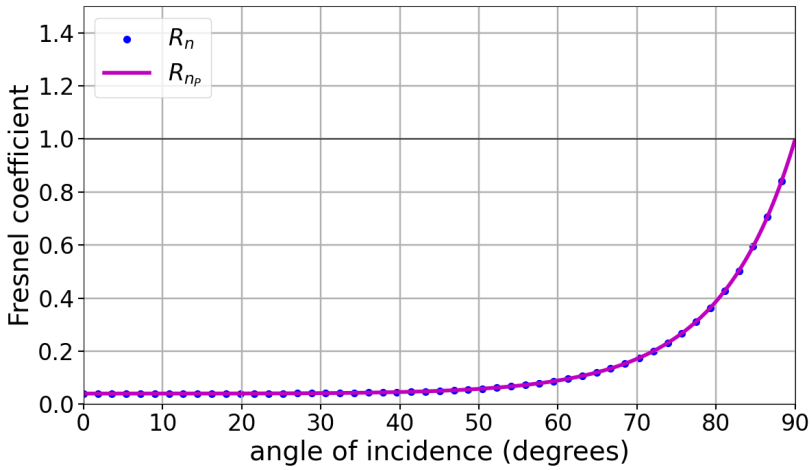

Figure A.3: Fresnel coefficients R_n and R_{n_P} are calculated for the specified NIM interface using Equations (4.16) and (A.1), respectively.

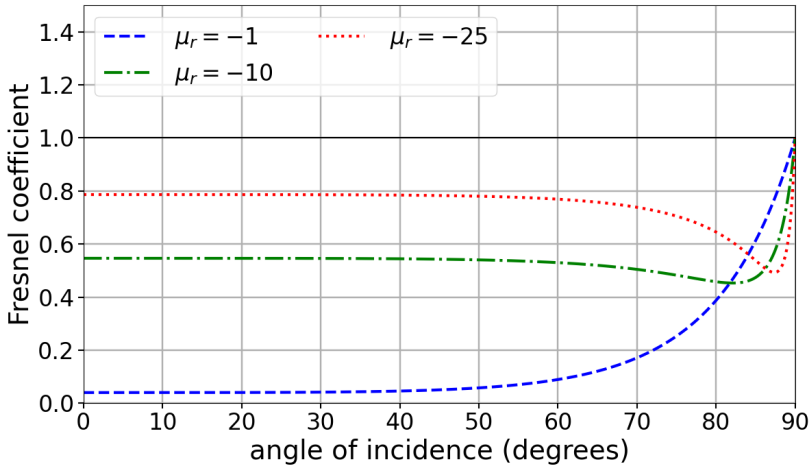

Figure A.4: Fresnel coefficients (R_n) calculated for the specified NIM interface using the described formulation and considering distinct relative permeability (μ_r) values.

While experimental results remain limited, the ability to engineer specific values of μ_r motivates the exploration of variations of this parameter, which is enabled by the described formulation (Equations (4.16), (4.17) and (4.18)). The graph presented in Figure A.4 illustrates the impact of these variations on R_n.

Appendix B

Ray Geometry Under Negative Refraction

Visualizations of negative refraction can appear counterintuitive due to their unconventional nature. In this context, ray diagrams can facilitate the clarification of the overall behaviour of light propagating across different optical scenarios. For instance, in Figure B.1, we present diagrams (obtained using Ray Optics Simulation software [50]) depicting directional light (parallel rays) incident on glass (left column) and NIM (right column) spheres, which are represented by circles in 2-D. At the air-sphere interfaces, fractions of the incident light are reflected and refracted according to the Fresnel equations. More specifically, we employed Equations (2.11) to (2.14) to compute the Fresnel coefficients for the air-glass interface, and Equations (4.16) to (4.15) and (4.21) to compute them for the air-NIM interface.

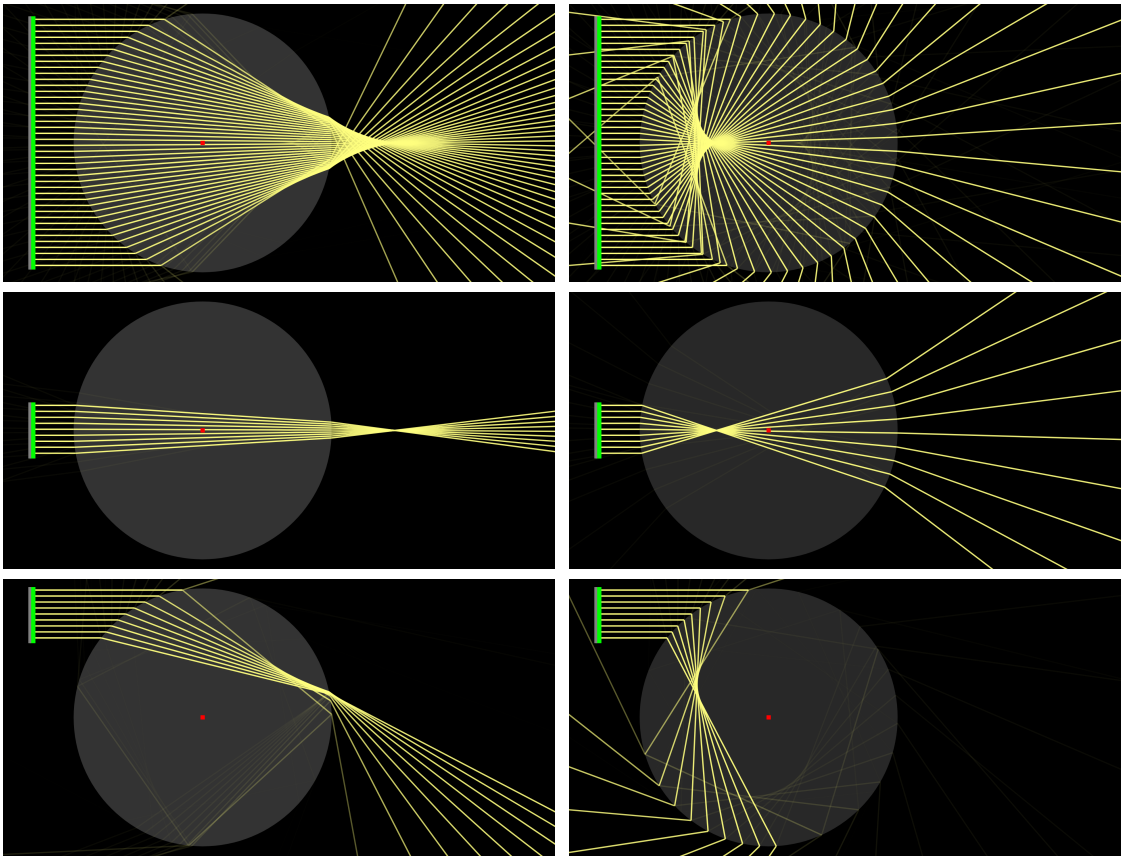

Figure B.1: A series of diagrams depicting parallel rays incident on spheres (represented as circles in 2D) surrounded by air ($\eta = 1$). Left column: glass spheres ($\eta = 1.5$). Right column: NIM spheres ($\eta = -1.5$). Top row: light incident on the left hemisphere. Middle row: light incident on a central region. Bottom row: light incident on a peripheral (off-axis) region. The vertical green bar represents the origin of the parallel rays, and the red dots represent the spheres' centres.

As it can be noted in the diagrams presented in Figure B.1 (top row), rays incident on the glass spheres' left hemisphere converge on the opposite side from the light source, producing a caustic pattern [51]. Conversely, the rays incident on the NIM sphere's left hemisphere diverge when emerging at the opposite side, and they do not create a bright region. Notably, the rays initially converge inside of the sphere before diverging outward. These aspects match the expectations of Veselago [52] that a structure producing converging behaviour as a conventional material would produce a diverging behaviour as a NIM, and vice-versa.

For the situation where the rays are incident on the spheres' central region, depicted in Figure B.1 (middle row), they converge on the opposite side of the light source after traversing the glass sphere, and diverge outwards on the opposite side from the light source after traversing the NIM sphere. In both cases, it is evident that incident light rays end up on the opposite side of the horizontal central axis of the sphere after emerging. Light rays incident on the top half of the NIM sphere end up traveling downwards, while light rays incident on the bottom half end up traveling upwards. As a result, in the central region of a NIM sphere, an observer positioned at the light source's location would see a vertically inverted image of objects positioned on the opposite side.

Lastly, as it can be seen in the ray diagrams for rays incident on a peripheral (off-axis) region of the spheres, as presented in Figure B.1 (bottom row), there is a significant difference in the behaviour of the materials. As expected, rays incident towards the top of the glass sphere converge on the opposite side from the light source and travel downwards after emerging. In the case of the NIM sphere, these incident rays emerge from the same

side of the sphere's surface where the light was incident. Therefore, an observer positioned at the light source's location would see objects positioned in the space between them and the sphere, or even objects positioned behind the observation plane when looking towards the NIM sphere's peripheral regions.

Index of Terms